JAMES | Journal of Advances in Modeling Earth Systems

RESEARCH ARTICLE
10.1029/2022MS003230

The Effect of Advection on the Three Dimensional Distribution of Turbulent Kinetic Energy and Its Generation in Idealized Tropical Cyclone Simulations

Joshua B. Wadler[1], David. S. Nolan[2], Jun A. Zhang[3,4], Lynn K. Shay[2], Joseph B. Olson[5], and Joseph J. Cione[4]

[1]Department of Applied Aviation Sciences, Embry-Riddle Aeronautical University, Daytona Beach, FL, USA, [2]Rosenstiel School of Marine, Atmospheric, and Earth Sciences, University of Miami, Coral Gables, FL, USA, [3]Cooperative Institute for Marine and Atmospheric Science, University of Miami, Coral Gables, FL, USA, [4]Atlantic Oceanographic and Meteorological Laboratory, Hurricane Research Division, NOAA, Miami, FL, USA, [5]Global Systems Laboratory, NOAA, Boulder, CO, USA

Key Points:

- The study determines how turbulent kinetic energy (TKE) advection influences tropical cyclone simulations subject to storm motion and ocean coupling
- The inclusion of TKE advection changes the storm-relative location of maximum TKE and the vertical distribution of TKE in each quadrant
- The inclusion of TKE advection produces a more realistic distribution of TKE and should be used in closure schemes when possible

Correspondence to:
J. B. Wadler,
wadlerj@erau.edu

Citation:
Wadler, J. B., Nolan, D. S., Zhang, J. A., Shay, L. K., Olson, J. B., & Cione, J. J. (2023). The effect of advection on the three dimensional distribution of turbulent kinetic energy and its generation in idealized tropical cyclone simulations. *Journal of Advances in Modeling Earth Systems*, *15*, e2022MS003230. https://doi.org/10.1029/2022MS003230

Received 8 JUN 2022
Accepted 30 APR 2023

Abstract The distribution of turbulent kinetic energy (TKE) and its budget terms is estimated in simulated tropical cyclones (TCs) of various intensities. Each simulated TC is subject to storm motion, wind shear, and oceanic coupling. Different storm intensities are achieved through different ocean profiles in the model initialization. For each oceanic profile, the atmospheric simulations are performed with and without TKE advection. In all simulations, the TKE is maximized at low levels (i.e., below 1 km) and ∼0.5 km radially inward of the azimuthal-mean radius of maximum wind speed at 1-km height. As in a previous study, the axisymmetric TKE decreases with height in the eyewall, but more abruptly in simulations without TKE advection. The largest TKE budget terms are shear generation and dissipation, though variability in vertical turbulent transport and buoyancy production affect the change in the azimuthal-mean TKE distribution. The general relationships between the TKE budget terms are consistent across different radii, regardless of storm intensity. In terms of the asymmetric distribution in the eyewall, TKE is maximized in the front-left quadrant where the sea surface temperature (SST) is highest and is minimized in the rear-right quadrant where the SST is the lowest. In the category-5 simulation, the height of the TKE maximum varies significantly in the eyewall between quadrants and is between ∼400 m in the rear-right quadrant and ∼1,000 m in the front-left quadrant. When TKE advection is included in the simulations, the maximum eyewall TKE values are downwind compared to the simulations without TKE advection.

Plain Language Summary Accurately predicting the distribution and transport of wind energy is important for accurate forecasting of hurricanes by computer models. This study aims to improve our understanding of the energy associated with small-scale eddies and gusts that are known as turbulence. Computer simulations were first analyzed to study the distributions of turbulent energy in the simulated hurricanes. The maximum of this energy is located below 1-km altitude and inward of the region of strongest winds. We examined how hurricane structure and intensity are affected by enabling the model to more realistically transport the turbulence and its energy. This energy transport increases the turbulence in upper levels of the strongest winds while reducing it near the surface. The transport of this energy also pushes the region of maximum turbulent energy downwind of its location without the transport being included. These changes made the simulated turbulent energy field more consistent with observations. This study suggests that enabling the realistic transport of turbulence will improve simulations and forecasts of hurricanes.

1. Introduction

Understanding the distribution of turbulent kinetic energy (TKE) in tropical cyclones (TCs) is critically important for improving subgrid-scale parameterizations in TC forecast models and advancing safety-related knowledge for flying crewed aircraft missions into TCs. While the lack of observations makes it challenging to produce and validate parameterizations of turbulent processes in the TC boundary layer (e.g., turbulent mixing of heat and momentum), these parameterizations are crucial for accurate TC forecasts in all numerical models (Zhang & Rogers 2019; Zhang et al., 2015, 2017). Numerical simulations of TCs are sensitive to the selection of surface flux parameterization (e.g., drag coefficient, exchange coefficient for enthalpy transfer) and boundary layer parameterizations (e.g., Braun & Tao, 2000; Emanuel, 1995; Green & Zhang, 2014; Katz & Zhu, 2017; Kepert, 2012;

Ming & Zhang, 2016; Montgomery et al., 2010; Nolan et al., 2009a, 2009b; Smith & Thomsen, 2010). Boundary layer parameterizations either include TKE advection (e.g., Mellor-Yamada-Nakanishi-Niino TKE scheme; called MYNN; Nakanishi & Niino, 2006, 2009; Olson et al., 2019) or do not have TKE advection available (e.g., Mellor-Yamada-Janjic TKE scheme; called MYJ; Janjic 1990, 1994, and the Yonsei University scheme; called YSU; Hong, 2010; Hong et al., 2006).

Since there are multiple boundary layer turbulence closures commonly utilized in numerical studies of TCs, it is important to describe how the distribution of TKE is influenced by the choice of turning TKE advection on or off. This was recently studied by X. Chen and Bryan (2021) in idealized simulations using Cloud Model 1 (CM1; Bryan & Fritsch, 2002). X. Chen and Bryan showed that including TKE advection led to a more realistic representation of TKE in the upper-level eyewall because of upward advection of TKE and concluded that TKE advection should be included in simulations of TCs. The simulations by X. Chen and Bryan, however, did not include ocean coupling, environmental vertical wind shear (the variation of horizontal winds with height), or storm motion, which all can contribute to storm-relative asymmetries of TKE. This manuscript builds on the results by X. Chen and Bryan (2021) by exploring how the inclusion of TKE advection influences the storm-relative asymmetric distribution of TKE and its budget terms.

Due to safety constraints, it is very difficult in TCs to directly observe properties of turbulence in atmospheric flows such as TKE, vertical and horizontal turbulent diffusion, and air-sea enthalpy fluxes. The first measurements of turbulence near a TC were during an aircraft stepped-descent in the periphery of Tropical Storm Eloise (1975) as presented in Moss and Merceret (1976, 1977) and in Moss (1978). Following that, the Coupled Boundary Layers Air-Sea Transfer (CBLAST) experiment was the next major research initiative aimed at measuring the properties of turbulence in the hurricane boundary layer (Bell et al., 2012; P. G. Black et al., 2007; Drennan et al., 2007; French et al., 2007; Zhang et al., 2008, 2009). The CBLAST experiment led to the first direct (in situ) measurements of humidity and momentum fluxes (Drennan et al., 2007; French et al., 2007; Zhang et al., 2009), sensible and latent heat fluxes from the ocean (Zhang et al., 2008), and vertical eddy diffusivity (Zhang & Drennan, 2012). Due to safety constraints of crewed aircraft, these measurements were made between rainbands, in wind speeds less than 30 m s^{-1}. Turbulence characteristics were calculated by Marks et al. (2008) for the inner-core of Hurricane Hugo (1989), before the enhanced safety constraints were in place, using 1 Hz flight-level data collected at ∼450 m. Marks et al. (2008) documented the structure and evolution of the eyewall vorticity maxima. Following the work by Marks et al. (2008), Zhang et al. (2011) estimated the TKE and momentum flux using data in Hurricanes Allen (1980) and Hugo (1989) at similar altitudes.

Properties of the turbulent flow have been estimated indirectly using remote sensing instruments. Using Doppler radar analyses, Lorsolo et al. (2010) estimated the TKE in several hurricanes. They found that the TKE is largest in the boundary layer and eyewall region. Recently, Sroka and Guimond (2021) calculated energy transfer and the full TKE budget in the boundary layer of Hurricane Rita (2005) using turbulence measurements from the Imaging Wind and Rain Airborne Profiler (IWRAP; e.g., Guimond, Sroka, & Proztko, 2018) instrument. They found that sub-filter-scale (SFS) energy transfer can have significant impact on the eddy flow and that turbulent eddies influence the TC vortex through wave-wave nonlinear interactions. Despite the availability of some measurements using remote sensing, the storm-scale distribution of TKE and the mechanisms of its generation and dissipation are still not well known.

Using CBLAST measurements, Zhang et al. (2009) produced the first TKE budget for the hurricane boundary layer. The largest contributor to TKE is vertical shear of the mean wind, while the largest sink is the dissipation of TKE. Both vertical turbulent transport and buoyancy production were small. Through an analysis of two aircraft legs, Sroka and Guimond (2021) found that both the turbulent transport and advective transport can be a significant TKE budget term whether or not the mean vortex is removed. Of note, the calculations by Sroka and Guimond are done in the eyewall of a hurricane as opposed to the outer rainbands as in Zhang et al. (2009). Pressure transport was not measured by Zhang et al. (2009) and is believed to be small (Donelan, 1990; Sroka & Guimond, 2021; Zhang, 2010). Zhang et al. noted that in the TKE budget, the dissipation term was larger than the shear production term and hypothesized that the radial advection of TKE in the inflow layer is important for balancing the budget. In a numerical modeling framework, Kepert (2012) confirmed that shear production is the dominant mechanism for TKE generation because of the large shear in wind speed near the surface (Kepert 2006a, 2006b). However, Kepert noted that buoyancy production (or loss) can become an important term for TKE budget near strong thermal gradients such as in regions of stable stratification (leading to destruction

Table 1
A List of the Spatial and Temporal Properties of Each Domain Used in the Model Simulation

	Domain 1	Domain 2	Domain 3	Domain 4 (inner-nest)
Domain size (longitudinal × meridional)	4,300 × 3,240 km	810 × 810 km	540 × 540 km	390 by 390 km
Horizontal resolution	27 km	9 km	3 km	1 km
Time step	60 s	20 s	6.67 s	3.33 s

of turbulence), and unstable stratification through strong buoyancy from surface heating (leading to creation of turbulence through free convection). The changing role of buoyancy production of TKE in different stability regimes has been confirmed in multiple studies (e.g., Hogstrom, 1990; Lenshow, 1970; Nicholls, 1985).

Due to the lack of observations, many questions remain about the distribution of TKE and its budget terms in TCs, especially at high wind speeds (>50 m s^{-1}). In addition, many questions remain about what distribution of turbulent properties is produced by operational models at high wind speeds, which are often built empirically based on low-wind conditions. This manuscript documents the three-dimensional distribution of TKE and its budget terms in idealized numerical TC simulations of different intensities, and how that distribution is influenced by the inclusion of TKE advection. The different storm intensities are realized through initializing the ocean with profiles that can reasonably simulate the sea surface temperature (SST) cooling underneath a TC. As in X. Chen and Bryan (2021), we perform simulations with TKE advection turned on or off to examine its role and importance for the simulated TC structure and overall TKE budget. The goals of the paper are as follows:

1. To understand how TKE advection affects the axisymmetric TC structure and TKE budget;
2. To document how the combined effects of storm-motion, SST cooling, and TKE advection influence the asymmetric distribution of TKE and its budget terms.

2. Methodology

This study utilizes the Advanced Research version of the Weather Research and Forecasting (WRF; Skamarock et al., 2008) model version 3.9.1.1. The model uses 40 vertical eta levels on four two-way nested domains (three following the vortex) with the innermost domain having a 1 km grid spacing. All domains are on an *f*-plane with a Coriolis parameter $f = 5 \times 10^{-5}$ s^{-1} (~20° N). The horizontal resolution of the other domains, grid sizes, and corresponding grid time steps are given in Table 1.

A weak 20 m s^{-1} idealized TC-like vortex with a radius of maximum winds (RMW) of 90 km is initialized using the method of point-downscaling (Nolan, 2011). Point-downscaling allows for a uniform atmospheric sounding and environmental vertical wind shear profile over the entire domain and has been used for a variety of TC numerical studies (e.g., Finocchio et al., 2016; Onderlinde & Nolan, 2014, 2016; Rios-Berrios et al., 2018). The idealized simulations also allow for an examination of how TKE and its generation is related to storm structure without external influences such as topography, mesoscale deformation, and dry air. The uniform atmospheric profile in this study is the Jordan mean sounding (Jordan, 1958) which has drier mid-levels than the Dunion moist-tropical sounding (Dunion, 2011). The drier mid-levels limit the intensity of our simulated TCs (e.g., M. Black et al., 2002; Braun et al., 2012; Gray, 1998; Kaplan & DeMaria, 2003; Tang & Emanuel, 2010, 2012) so that they are more consistent with typically observed storms. The environmental vertical wind shear is set to a constant 5 m s^{-1} (~10 knots) with 4 m s^{-1} easterly surface winds decreasing sinusoidally to 1 m s^{-1} westerly winds aloft (see Figure 2b in Nolan, 2011 but with the winds shifted 1 m s^{-1}). The environmental winds lead to a slow-moving vortex and allows for asymmetries due to SST cooling in the rear of the vortex (e.g., P. G. Black, 1983; Greatbatch, 1983; Jacob et al., 2000; Price, 1981; Shay et al., 2000) and asymmetries due to the vortex response to the environmental vertical wind shear (e.g., Reasor et al., 2013; Rogers et al., 2013; Wadler et al., 2018; Zhang et al., 2013).

The atmosphere is coupled to the 3-dimensional Price-Weller-Pinkel (3DPWP; Price, 1981; Price et al., 1994) ocean mixed layer model that is initialized with a horizontally uniform temperature profile. The 3DPWP scheme was integrated into WRF by Lee and Chen (2012) and accounts for vertical mixing, lateral advection, and vertical diffusion near the ocean surface. Three uniform ocean profiles are used for creating storms with different intensities: a warm-core oceanic eddy (WCE), a cold-core oceanic eddy (CCE), and an average profile between the WCE

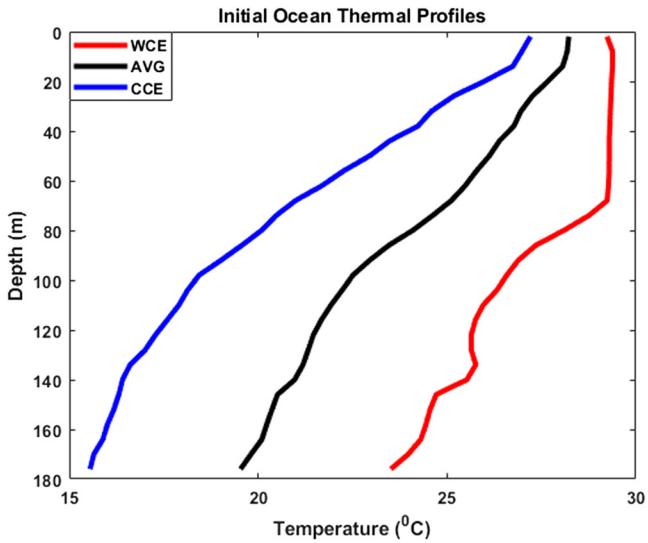

Figure 1. Temperature profiles of the warm core eddy (WCE), cold core eddy (CCE), and average profile between CCE and WCE (AVG) used to uniformly initialize the ocean in the Weather Research and Forecasting model.

and CCE (AVG). The ocean profiles also allow for a realistic cold-wake in the rear of the simulated TCs which affects TKE asymmetries. The initial temperature profiles are shown in Figure 1. The CCE and WCE profiles were taken before Hurricane Rita (2004) and are presented in Jaimes and Shay (2009). The ocean model uses 30 vertical levels with vertical resolution of 6 m. The WCE ocean initialization is designed to produce a hurricane of category-5 intensity (CAT5), while the CCE ocean initialization is designed to produce a hurricane of category-1 intensity (CAT1) and the AVG ocean profile is designed to produce a TC with an intensity between CAT5 and CAT1 (MID). For each oceanic profile, a simulation is performed with TKE advection (in the atmospheric model) by the total wind field (CAT5-WA, MID-WA, CAT1-WA) and without TKE advection (CAT5-NA, MID-NA, CAT1-NA). A list of all the simulations is given in Table 2.

For these idealized simulations, both the shortwave and longwave radiation parameterizations are turned off. The Kain–Fritsch cumulus Scheme (Kain, 2004) is used only on the outer domain, the microphysics scheme is the WRF single moment class 5 scheme (Hong et al., 2004), the surface layer parameterization is based on the implementation of MM5 Monin-Obukhov similarity theory (Beljaars, 1994; Dyer & Hicks, 1970; Paulson, 1970) with a drag coefficient that levels off at higher wind speeds (e.g., Donelan et al., 2004; Powell et al., 2003) following the recommendations of Green and Zhang (2014).

The boundary-layer parameterization is the Mellor-Yamada-Nakanishi-Niino level 2.5 TKE scheme (MYNN; Nakanishi & Niino, 2006, 2009) which explicitly solves the 1-D TKE equation given by Equation 1, with TKE defined by Equation 2:

$$\frac{\partial(2\cdot \mathrm{TKE})}{\partial t} = -\frac{\partial}{\partial z}\left\langle w\left(u^2+v^2+w^2+2\frac{p}{p_0}\right)\right\rangle - 2\left(\langle uw\rangle\frac{\partial U}{\partial z}+\langle vw\rangle\frac{\partial V}{\partial z}\right)+2\frac{g}{\theta_0}\langle w\theta_v\rangle - 2\varepsilon \quad (1)$$

$$\mathrm{TKE} = \frac{1}{2}\left(u^2+v^2+w^2\right) \quad (2)$$

where u,v,w are the zonal, meridional, and vertical velocities respectively, θ_v is virtual potential temperature, θ_0 is a reference potential temperature, and ε is parametrized dissipation. Capital letters represent the resolved volumetric (model grid cell) mean values while lower case letters represent the subgrid-scale (non-resolved) turbulent (deviation from mean) values. Angled brackets represent the model volume grid cell averages of the subgrid-scale turbulent fluxes. The left-hand side of Equation 1 represents total change in TKE, while the terms on the right-hand side represent vertical turbulent transport, shear production, buoyancy production or loss, and dissipation. Of note, the vertical turbulent transport term also includes turbulent pressure transport, which is usually considered negligible. The TKE budget terms are available as output from the MYNN scheme in WRF (Olson et al., 2019). Higher-order turbulence terms such as the time tendency of the covariance of virtual

Table 2
A Description of the Initial Ocean Profile and Use of Turbulent Kinetic Energy Advection for All the Simulations Utilized in This Study

Simulation	Ocean initialization	Turbulent kinetic energy advection
CAT5-WA	Warm-core eddy	Yes
CAT5-NA	Warm-core eddy	No
CAT1-WA	Cold-core eddy	Yes
CAT1-NA	Cold-core eddy	No
MID-WA	Average between cold-core eddy and warm-core eddy	Yes
MID-NA	Average between cold-core eddy and warm-core eddy	No

potential temperature and total water content are parameterized (Nakanishi & Niino, 2009). Of note, X. Chen and Bryan (2021) used a modified MYNN level 3 scheme to describe the TKE evolution which uses predictive equations for the second-order turbulent quantities. Previous studies have shown that the differences between the level 2.5 and 3.0 level schemes is small in most weather regimes (e.g., Nakanishi & Niino, 2009; Zhang et al., 2020; Zhu et al., 2014). The differences are generally assumed small in TC conditions, where shear production of TKE is expectedly much more significant in regulating total mixing than higher-order counter-gradient terms.

The MYNN scheme also allows for TKE advection to contribute to the TKE budget. With TKE advection turned on, the TKE at each time step is simultaneously updated and advected by the total wind field which does not allow us to quantify the direct contribution of TKE advection. To overcome this limitation and create a TKE budget, the TKE advection term is estimated as the difference between the sum of the TKE source terms (vertical turbulent transport, shear production, buoyancy production, and dissipation) and the total change in TKE. The total change in TKE is estimated by the difference in TKE between two model time steps. Unfortunately this approach does not allow for a separation of vertical and horizontal advection. While obtaining direct output of every TKE budget term would be desirable, this approach still yields valuable information about the relative roles of each term and how they relate to the mean vortex. In simulations with TKE advection turned off, the total change in TKE is equivalent to the local tendency and is defined as the sum of the four TKE budget terms on the right-hand side of Equation 1.

It is also worth noting that Equation 1 neglects all 3-D contributions to TKE. There is a rich literature of the 1-D versus 3-D forms of the TKE equation and attempts to modify planetary boundary layer schemes to perform better in intermediate scales with horizontal grid spacing between ∼200 and ∼1,000 m (these scales are referred to as *terra-incognita*; Efstathiou et al., 2016; Honnert & Masson et al., 2014; Wyngaard, 2004). Since the model grid spacing used in this study stays outside the commonly accepted region of *terra-incgonita*, an additional investigation to the impacts of neglecting the horizontal contributions is best reserved for a study that samples higher-resolution model configurations.

Though there are many differences between the MYNN boundary layer scheme and the more commonly used Mellor-Yamada-Janjic TKE closure scheme (MYJ; Janjic 1990, 1994), the primary difference is that the former uses effects of stability on the turbulent length scale and closure constants that are obtained from LESs. This leads to an improved representation of TKE over a larger range of stability regimes. Another significant difference is that the MYNN scheme has a diagnostic equation for the turbulent length scale which, along with the TKE, is commonly underestimated in the MYJ scheme (Nakanishi & Niino, 2009). The MYJ scheme does not have the option for TKE advection.

The analysis of the TKE and budget terms from the MYNN boundary layer represents an estimation of the turbulence distribution at a wide range of wind speeds. While the MYNN scheme is formulated empirically using low-wind data, it, or any boundary layer closure scheme employed in operational and research settings, have no choice but to parameterize all weather conditions. Given the common use of turbulence closures, it is important to investigate its behavior in both verified and unverified regimes. For example, using a large eddy simulation (LES) over a small region of Hurricane Ivan, Zhu (2008) showed that boundary layer schemes underestimate TKE values because they do not include turbulent transport of TKE. However, the LES of Zhu (2008) was over land, which has a larger drag coefficient than the ocean. While LES can provide an explicit solution over a larger range of the energy-containing turbulent eddies that populate the TC boundary layer than the MYNN scheme, their use is still limited by computational power with most simulations of TCs having a limited integration time and a domain that does not extend outward far beyond the eyewall region (Green & Zhang, 2015; Rotunno et al., 2009). The WRF simulations in this study provide a modeling-based estimate of turbulence characteristics in the context of larger-scale storm structure and characteristics.

The performance of the MYNN boundary layer scheme (without TKE advection) for simulating hurricanes was examined in two previous studies. Green and Zhang (2014) found that the MYNN boundary layer, in combination with the surface layer parameterization used in this study, leads to a reasonable simulation of observed boundary layer structure. Zhu et al. (2014) also showed that the MYNN parameterizations produce reasonable boundary layer structure but found that both the MYNN level 2.5 and 3.0 closures tend to suppress smaller-scale perturbations such as eyewall mesovortices. Note that the Zhu et al. (2014) study was performed before TKE advection was included in the MYNN boundary layer scheme that is available in WRF3.9.1.1.

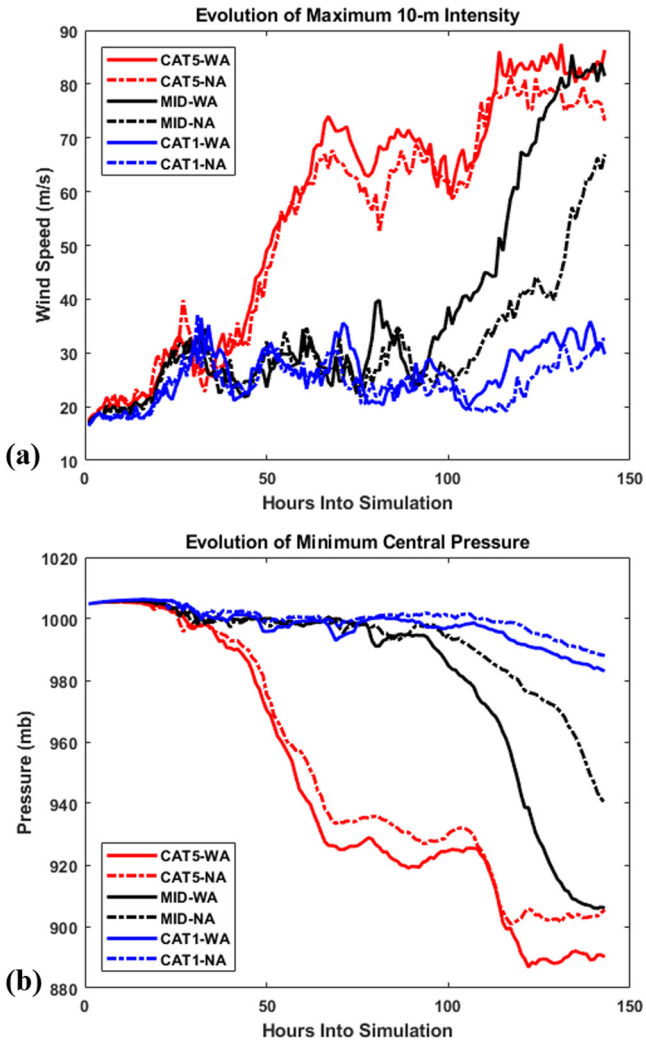

Figure 2. The evolution of (a) maximum 10-m wind speed and (b) minimum central pressure for the six simulations used in this study. The solid lines represent simulations with turbulent kinetic energy (TKE) advection while the dashed lines represent simulations without TKE advection.

3. Results

Time series of maximum 10-m wind speed and minimum surface pressure for each of the simulations are shown in Figure 2. Each simulated TC underwent significant intensification, except those over the CCE ocean (CAT1 simulations). The different onset times of the intensification between the AVG ocean (MID simulations) and the WCE ocean (CAT5 simulations) runs was related to the oceanic profiles, with the warmer ocean unsurprisingly leading to more rapid TC development. For each ocean profile, the simulation with TKE advection had stronger 10-m winds and lower surface pressure than that without TKE advection, a result similar to that from X. Chen and Bryan (2021).

The two CAT5 simulations produced extremely intense storms with minimum surface pressures between 890 and 905 mb and 10-m wind speeds exceeding 75 m s^{-1}. The extreme intensities are expected since the environmental shear is low, there is no dry air near the TCs, and the SSTs always exceed 28°C. To explore the differences in the model produced near steady-state structure of TKE and the influence of TKE advection on overall TC structure at both low and high wind speeds, the analysis hereafter focuses on the CAT1 and CAT5 simulations. All four of these simulations maintain nearly steady-state intensities over the last 24 hr, allowing for an analysis of the relationship between TKE and the mean vortex structure. To account for the intensity differences between the simulations with/without TKE advection, all of the analyses will be normalized relative to either the maximum TKE values or the maximum wind speed values (discussed later). The MID simulations contain signals that closely resemble that of the CAT5 simulations, though there are large differences between the MID-WA and MID-NA simulations due to their different intensities.

3.1. TKE and Mean-Vortex Structure

To sample the representative eyewall values of TKE, we sample the hourly recordings of TKE (after 72 hr into the simulations) at the location of maximum wind speed at 600-m altitude. Qualitatively, there is good agreement between the TKE from the CAT1-WA simulation and the observational estimates of TKE in wind speeds between 20 and 30 m s^{-1} presented in Zhang et al. (2011) from flight level data at a similar altitude in two storms (Figure 3). Note that the TKE calculated by Zhang et al. was based on the eddy correlation method using a time average of 3D wind data when the P-3 was flying at a constant altitude which were legs between 20 and 30 km in length. Zhang et al. (2011) found that the TKE in the eyewall is dominated by eddies with horizontal length scales between 500 and 3,000 m. To ensure equal comparison between the model produced TKE and that based on observations, we further filtered the data from Zhang et al. (2011) to only include scales of 2 km or below. In our simulations, the TKE variable is intended to represent the total energy of all sub-grid scale eddies, which may include eddies up to 2 grid spacings (2 km) in size. As discussed in Wyngaard (2004), most of the energy in boundary layer turbulence is in the larger scale eddies. Therefore, while we cannot say for certain that the model TKE corresponds exactly to the length scales reported by Zhang et al., there is considerable overlap. At higher wind speeds between 40 and 65 m s^{-1}, the TKE from the CAT5-WA simulation also has some agreement with the estimates from Zhang et al. (2011), though there is less observational data in that range. The model-produced TKE is also within the bounds of that estimated from the recently deployed Coyote uncrewed aircraft system (UAS) over a wide range of wind speeds in two hurricanes (see Cione et al., 2020 for details).

It is worth noting that the MYNN TKE output is from subgrid-scale processes and does not include TKE resolved on the model grid scale. Thus, the TKE shown in this study focuses on what was generated at horizontal spatial scales of less than 2 km, close to typical scales of coherent turbulent eddies or rolls (e.g., Foster 2013; Guimond,

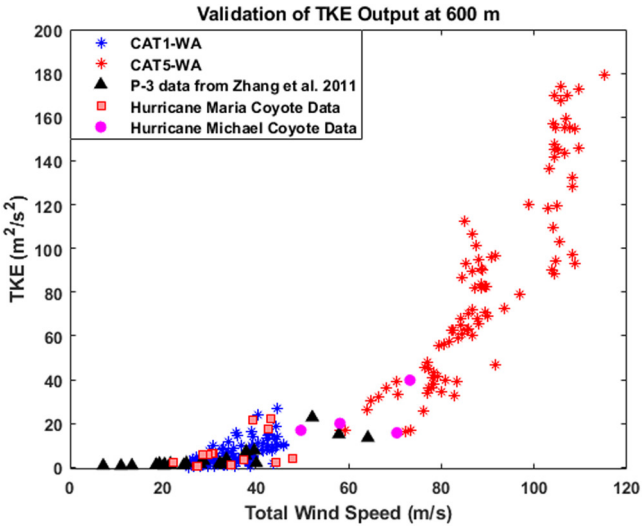

Figure 3. Comparison between the turbulent kinetic energy (TKE) estimated from flight-level data obtained in Hurricanes Hugo (1989) and Allen (1980) that is presented in Zhang et al. (2011), and that produced at 600-m altitude (similar height to aircraft measurements) by the MYNN boundary layer parameterization in Weather Research and Forecasting for the CAT5-WA and CAT1-WA simulations. Estimated TKE from the Coyote uncrewed aircraft system in Hurricanes Maria (2017) and Michael (2018) are also overlaid.

Zhang, et al., 2018; Lorsolo et al., 2008; Sroka & Guimond, 2021; Zhang et al., 2008). The high values of TKE in the CAT5 simulation at wind speeds greater than 75 m s^{-1} have not been observed, signifying that the TKE distribution at high winds is a purely model-based estimate. While turbulence closure schemes such as MYNN are not designed for these extreme values, they are commonly used in operational and research models. Thus, even with inherent limitations and uncertainty at high winds, we conclude that the model output of TKE provides a sensible distribution that is in agreement with observational estimates at wind speeds less than 75 m s^{-1} and warrants further exploration of its characteristics and relationship to vortex structure at different wind speeds.

To explore how the TKE distributions are related to vortex-scale storm features, and to avoid transient convective and mesoscale features biasing our results, the azimuthally averaged TKE from hourly output is averaged over the last 24 hr of the simulations. The TKE distributions are also normalized relative to the maximum axisymmetric TKE value to control for differences in storm intensity. The CAT5-WA simulation (Figure 4a) has a TKE maximum located at ∼1-km altitude, above the region of radial wind convergence and maximum tangential wind speed. The TKE maximum is also radially inward of the 1-km altitude RMW, and near the base of the eyewall updrafts. The TKE in the eyewall decreases to ∼10% of the maximum value by 7-km altitude, but its maximum remains inside the RMW. Interestingly, away from the eyewall TKE greater than 10% of its peak value extends ∼0.5 km above the inflow layer out to a 70 km radius.

In the CAT5-NA simulation (Figure 4b), the TKE maximum is at a slightly lower altitude than in the CAT5-WA simulation, but is at a similar location relative to the maximum tangential wind speed and region of radial wind convergence. The most significant difference in the distribution of the TKE between the CAT5 simulations is in the mid-to-upper levels of the eyewall. The TKE in the CAT5-NA simulations becomes lower than 10% of its peak value at ∼3.5 km altitude. The non-negligible TKE values at the mid-to-upper levels of the eyewall in the CAT5-WA simulation are closer to patterns derived by observations by Lorsolo et al. (2010) than the CAT5-NA simulation, and reinforces the results from X. Chen and Bryan (2021) with a different dynamical core, grid spacing in the innermost domain (3.0 km in X. Chen and Bryan vs. 1.0 km in this study), and initial conditions. X. Chen and Bryan (2021) linked the enhanced TKE in the mid-to-upper levels of the eyewall to greater upward water vapor transport in the eyewall and enhanced diabatic heating to explain how the simulations with TKE advection create a stronger vortex.

In both CAT1 simulations (Figures 4c and 4d), the TKE maximum is in the low-level (∼300 m) eyewall and the region of radial wind convergence. As with the CAT5-NA simulation, the lack of TKE advection in the CAT1-NA simulation limits the vertical extent that the TKE reaches in the eyewall. The TKE in the CAT1-WA simulation decreases to 10% its peak value at ∼2.0 km in the eyewall, while the TKE in the CAT1-NA simulation only extends upwards to ∼1.0-km altitude. The results highlight the very low levels of turbulence in the middle and upper levels of a minor hurricane. Even so, individual convective cells within the vortex may still contain significant TKE.

3.2. Axisymmetric TKE Budget

As X. Chen and Bryan (2021) focused on how the inclusion of TKE advection influences TC intensity, we show how TKE advection influences the spatial distribution of the TKE budget terms. Radius-height cross sections of the azimuthally averaged TKE budget terms in the CAT5-WA simulation are presented in Figure 5. Consistent with previous studies, the two largest terms in the TKE budget are shear production (positive generation; Figure 5a) and dissipation (negative generation; Figure 5b). Both shear generation and dissipation are maximized along the axis of maximum TKE, which is radially inward of the RMW above ∼500 m altitude. On average, the buoyancy production term only contributes negatively to TKE tendency (a similar result was found in X. Chen & Bryan, 2021) and is maximized at ∼2 km altitude along the axis of maximum TKE. Positive buoyancy production

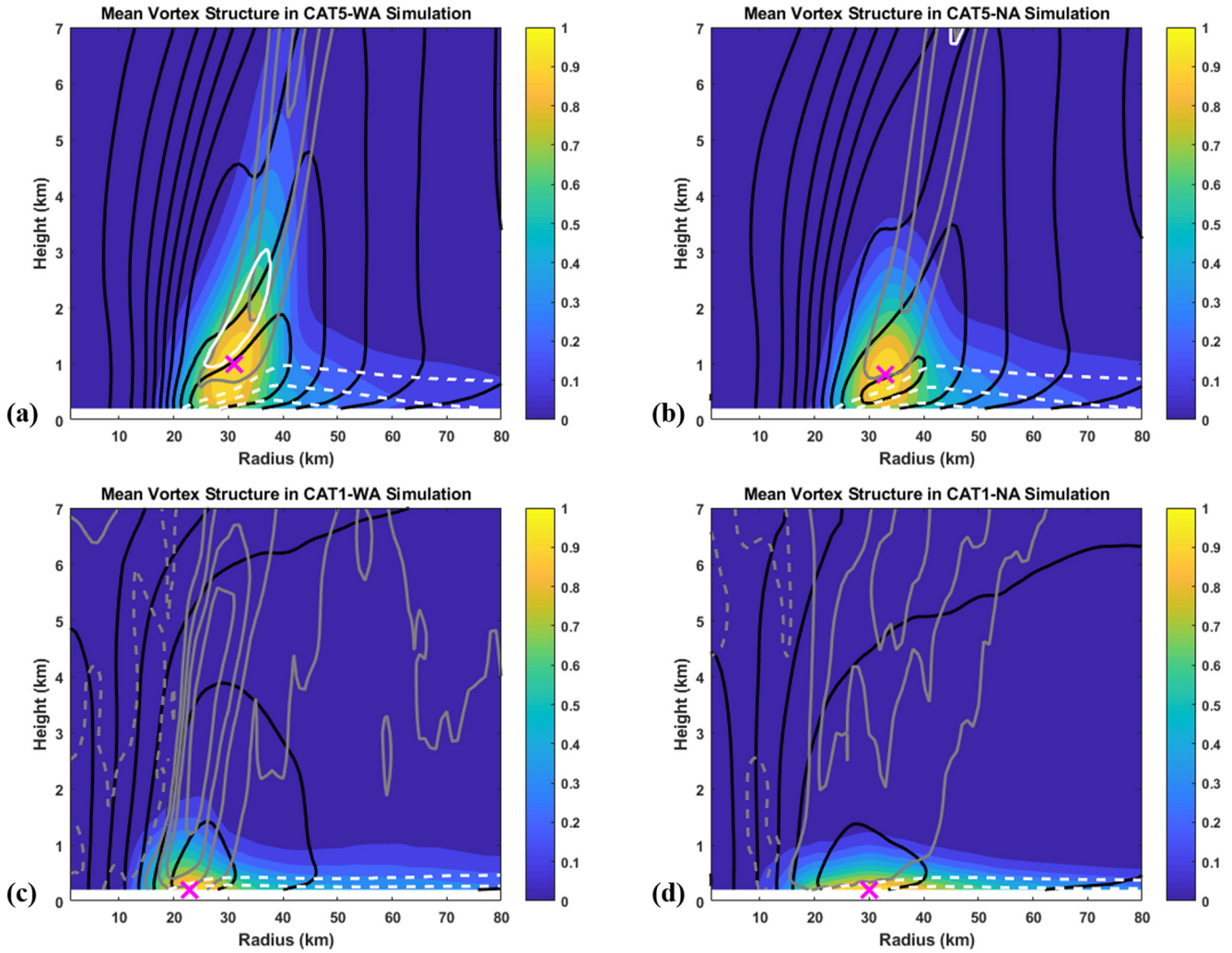

Figure 4. Azimuthally averaged turbulent kinetic energy (TKE; shaded) normalized by its maximum value, tangential wind (black contour), radial wind (white contour; inflow = dashed line, outflow = solid line), and vertical velocity (gray contour; positive = solid line, negative = dashed line) for the (a) CAT5-WA, (b) CAT5-NA, (c) CAT1-WA, and (d) CAT1-NA simulations, averaged over the last 24 hr. For each panel, the red "x" represents the maximum TKE. In (a) and (b) the contour interval is 0.1 for normalized TKE, 10 m s^{-1} for tangential wind, 5 m s^{-1} for radial wind and 2 m s^{-1} for vertical velocity. In (c) and (d) the contour interval is 0.1 for normalized TKE, 5 m s^{-1} for tangential wind, 2 m s^{-1} for radial wind, and 0.1 m s^{-1} for vertical velocity.

tends to occur over small areas near spiral rain bands (not shown). The vertical turbulent transport tendency is negative in the eyewall below ∼500 m altitude, but positive between ∼500 and ∼1,000 m at most radii. Above the boundary layer, there is positive vertical turbulent transport tendency along the RMW up to 7 km altitude, with slightly negative vertical turbulent transport tendency elsewhere. Below ∼1–1.5 km altitude, TKE advection (Figure 5e) contributes negatively to the mean TKE change since the radial wind advects lower TKE values toward the storm center. Above ∼1.5 km of the eyewall, TKE advection contributes positively to TKE tendency and is responsible for the enhanced eyewall TKE observed in Figure 4a.

As the simulated TCs are not exactly in steady-state over the analysis period, there are changes in the azimuthal-mean TKE. In the CAT5-WA simulation (Figure 5f) the mean TKE change (i.e., the evolution of the azimuthal-mean state of the TKE from the beginning to the end of the analysis period) is maximized at the base of the eyewall, with positive values of TKE tendency below ∼1,500 m altitude extending beyond a radius of 80 km. Though most of the domain above the inflow layer experiences TKE reduction, the most significant reduction is seen in the eyewall between ∼2 and 6 km altitude. The TKE budget terms in the CAT5-NA simulation maintain similar characteristics, but with a lesser vertical extent of TKE in the lower troposphere than in the CAT5-WA simulation (not shown). The similarity of the distributions is reflected in the mean TKE change

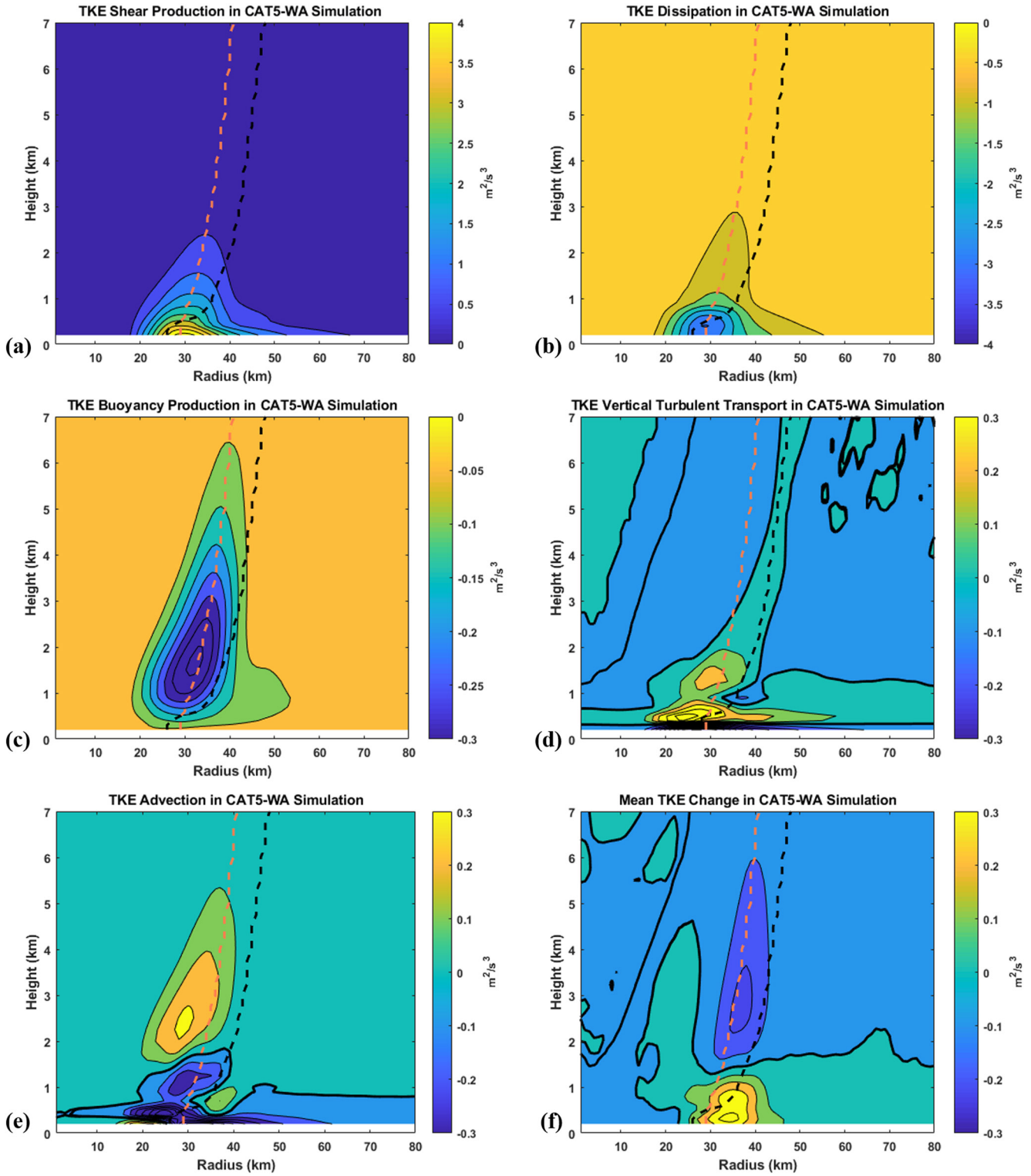

Figure 5. Azimuthally averaged (a) turbulent kinetic energy (TKE) shear production, (b) TKE dissipation, (c) TKE buoyancy production, (d) TKE vertical turbulent transport, (e) TKE advection, and (f) total change in TKE, averaged over the last 24 hr of the CAT5-WA simulation. The contour intervals are (a) 0.5 $m^2 s^{-3}$, (b) 0.5 $m^2 s^{-3}$, (c) 0.05 $m^2 s^{-3}$, (d) 0.1 $m^2 s^{-3}$, (e) 0.2 $m^2 s^{-3}$, and (f) 0.1 $m^2 s^{-3}$. In each panel, the dashed black line represents the radius of maximum winds and the orange dashed line represents the axis of maximum TKE. The thick black line in (d), (e), and (f) represent the zero contour of the TKE budget term of that respective panel.

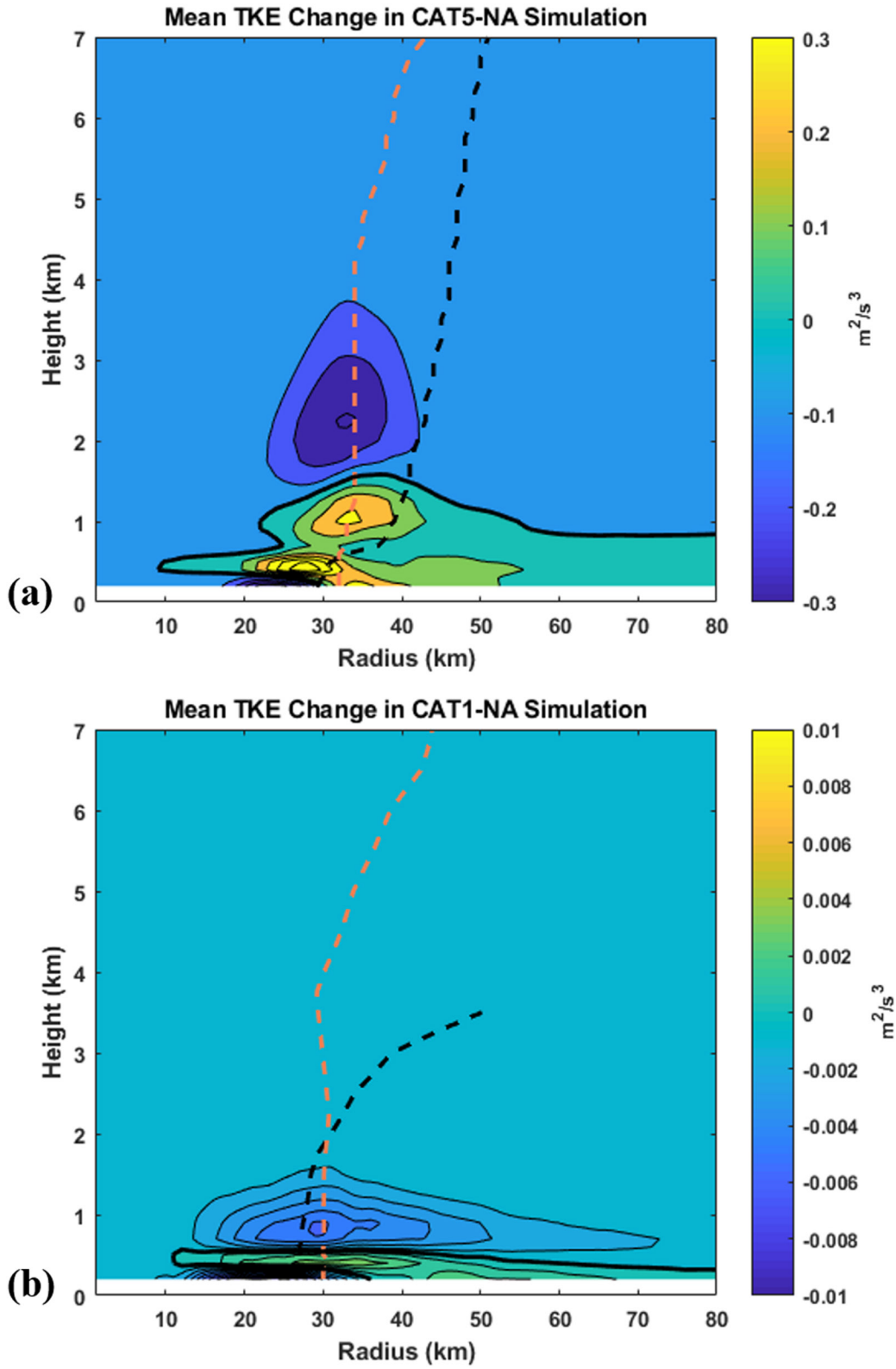

Figure 6. Azimuthally averaged (a) total change in turbulent kinetic energy (TKE) in CAT5-NA simulation and (b) total change in TKE in CAT1-NA simulation, averaged over the last 24 hr of the respective simulations. The contour interval is (a) 0.1 $m^2\ s^{-3}$ and (b) 0.001 $m^2\ s^{-3}$. In each panel, the dashed black line represents the radius of maximum winds, the orange dashed line represents the axis of maximum TKE, and the thick black line represents the zero contour.

in the CAT5-NA simulation (Figure 6a). The most significant difference in the mean TKE change between the two CAT5 simulations is in the eyewall between 2 and 3 km altitude. In this region, the lack of TKE advection in CAT5-NA leads to more TKE destruction in the CAT5-NA simulation than in the CAT5-WA simulation, an important result that directly leads to less turbulence within the mid-to-upper levels of the eyewall.

As with the CAT5-WA simulation, the two TKE budget terms with the largest magnitudes in the CAT1-WA simulation are shear production (Figure 7a) and dissipation (Figure 7b). However, in the CAT1-WA simulation, these terms are generally confined to the lowest ∼1 km. Both terms are maximized at the nearly co-located low-level RMW and axis of maximum TKE. The negative buoyancy production (Figure 7c) is confined to the lowest ∼3 km of the eyewall, a lesser vertical extent than in the CAT5-WA simulation where the term reaches ∼6.5 km altitude. However, the negative buoyancy production term in the CAT1-WA simulation extends beyond 80 km radius, while in CAT5-WA simulation its radial extent is ∼55 km before dropping below 5% of its peak value. The vertical turbulent transport term (Figure 7d) has similar characteristics as in the CAT5-WA simulation, but in the CAT1-WA simulation there is no significant vertical turbulent transport along the RMW above ∼2 km altitude. TKE advection (Figure 7e) leads to a reduction of TKE below ∼700 m altitude from the eyewall to a radius of 80 km, but enhances it above. Positive TKE advection is maximized in the eyewall at ∼1 km altitude.

The mean TKE change in the CAT1-WA simulation (Figure 7f) shows positive generation confined to the lowest 500 m of the eyewall from the eyewall to 80 km radius. There is an elongated area of negative generation maximized 10 km radially inward of the RMW between ∼500-m and ∼2-km altitudes. As with the CAT5 simulations, all the TKE budget terms in the CAT1-NA simulation have similar characteristics as the CAT1-WA simulation (not shown). Similarly, the lack of TKE advection leads to a greater reduction of TKE above the inflow layer in the CAT1-NA simulation (Figure 6b) than in the CAT1-WA simulation.

The terms are grouped into 10-km wide radial bins centered on the 500-m altitude RMW to further explore the distribution of the TKE budget over the last 24 hr of each simulation. The bins are used for averaging 5 km radially inward and outward of the RMW. Since the axis of maximum TKE is not necessarily co-located with the RMW, the bins do not represent the maximum magnitude of the TKE budget terms. However, centering the terms on the RMW is useful since it relates the TKE budget to the mean vortex structure and creates a common reference point among the simulations. Figure 8 shows the mean and two standard errors based on the variance of the sample (shading) of each TKE budget term up to 3-km altitude. Only the lowest 3 km are shown since TKE values are generally small above 3 km and these radial bins do not incorporate the eyewall tilt.

The magnitudes of the shear production and dissipation below 0.5 km are ∼0.5–1.5 $m^2 s^{-3}$ greater in the CAT5-WA simulation (Figure 8a) than in the CAT5-NA simulation (Figure 8b). The difference in magnitude likely reflects the higher mean values of TKE in the CAT5-WA simulation. The magnitudes of the shear production and dissipation terms are more than double the magnitudes of the vertical turbulent transport, buoyancy production, and TKE advection terms. However, the difference between the shear production and dissipation is comparable to other budget terms, meaning variations in all terms are important for determining the total TKE change. Below ∼500 m, the vertical transport and buoyancy terms maintain similar magnitudes between the CAT5-WA and CAT5-NA simulations, meaning that for the similar total TKE change, the shear production must increase more than the dissipation to account for the negative effects of TKE advection.

As shown in the azimuthally averaged cross sections, the vertical turbulent transport term in the CAT5 simulations is negative below ∼400 m and positive above. The buoyancy production term is always negative, and its magnitude maximizes at ∼1.5-km altitude. In the lowest 500 m, the net production of TKE in the eyewall is similar between CAT5-WA simulation and the CAT5-NA simulation due to the negative contribution from the TKE advection to the total TKE change in the low levels. Above ∼1,500 m, the mean TKE change is more negative in the CAT5-NA simulation than in the CAT5-WA simulation, a result driven by the differences in the TKE advection term.

The CAT1 simulations (Figures 8c and 8d) maintain similar characteristics, though the TKE terms are nearly two orders of magnitude less than those for CAT5. In the CAT1 simulations, there is no positive eyewall net TKE generation above 500 m, suggesting that the strong wind shear of the vertically varying tangential flow in the CAT5 runs can significantly change the relative distribution of budget terms. As in the CAT5 simulations, the magnitude of the TKE budget terms in the CAT1 simulations decay with height, and at a larger rate in the simulation without TKE advection. The largest differences in TKE tendency with height are a positive production at ∼500 m and negative production between ∼600 and 1,500 m in the CAT1-NA simulation. Neither of those maxima are present in the CAT1-WA simulation, due to the inclusion of TKE advection.

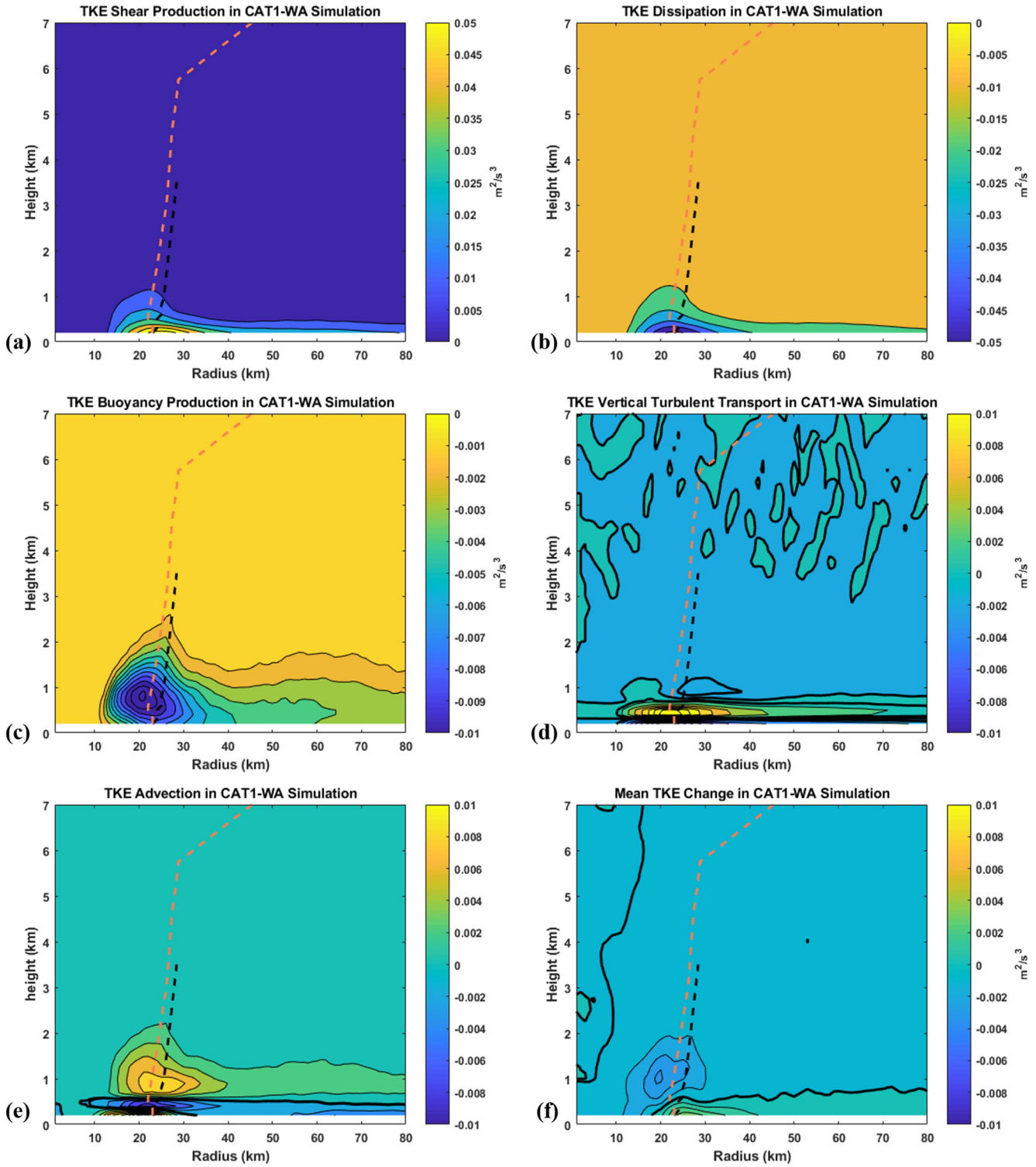

Figure 7. As in Figure 5, but for the CAT1-WA simulation. The contouring interval in these panels are: (a) 0.01 m^2 s^{-3}, (b) 0.01 m^2 s^{-3}, (c) 0.001 m^2 s^{-3}, (d) 0.002 m^2 s^{-3}, (e) 0.002 m^2 s^{-3}, and (f) 0.001 m^2 s^{-3}.

The same statistical analyses were performed for radial bins centered between 10 and 50 km outside of the RMW (not shown). While the magnitude of the TKE budget terms decreases with increasing radius, the absence of vertical advection in the areas away from the eyewall means that the general relationship between the budget terms with height remains largely unchanged with increasing radius. By 50-km away from the eyewall, the terms were

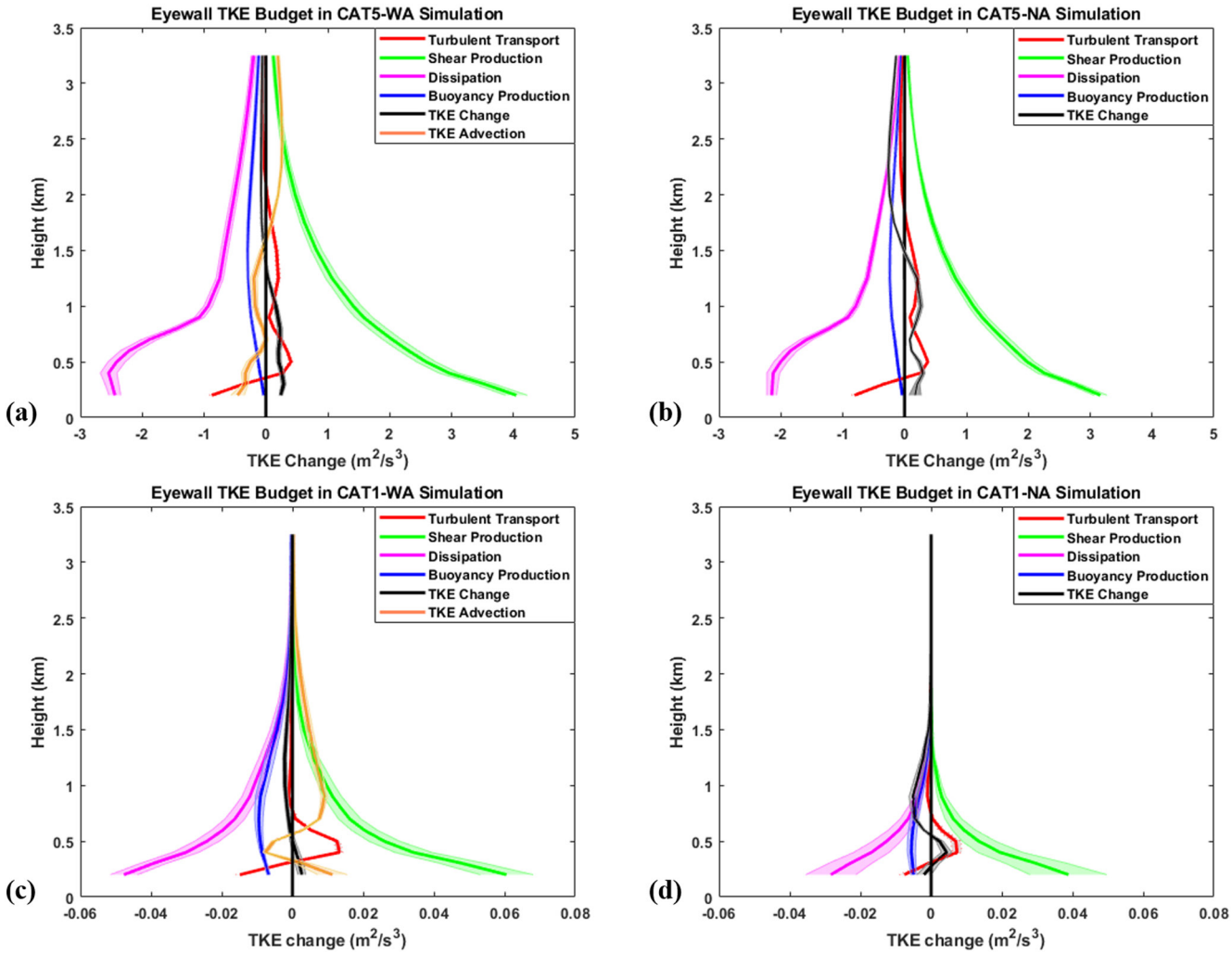

Figure 8. Mean and two standard errors (shaded) of all turbulent kinetic energy budget terms in the (a) CAT5-WA, (b) CAT5-NA, (c) CAT1-WA, (d) CAT1-NA simulations. The terms are centered at the 500 m radius of maximum winds in each simulation and averaged 5 km radially inward and outward.

only ∼10%–20% the magnitude that they were near the eyewall. With the consistent relationships between the budget terms, the largest differences in the total change in TKE change in the boundary layer due to the inclusion of TKE advection are located just radially inward of the low-level RMW (i.e., Figure 5f vs. Figure 6a for CAT5 simulations and Figures 7f and 6b for the CAT1 simulations), a similar result to X. Chen and Bryan (2021).

3.3. Storm-Relative Asymmetries of TKE

As stated earlier, a significant difference between this manuscript and that of X. Chen and Bryan (2021) is the inclusion of asymmetries in the simulated TCs due to storm-motion, environmental wind shear, and SST cooling. Here, the TKE distribution is divided into storm-motion relative quadrants. Previous studies show that SST cooling due to storm motion can lead to suppressed air-sea temperature and humidity contrasts, lower enthalpy fluxes, and create a locally stable boundary layer (e.g., S. S. Chen et al., 2013; Cione, 2015; Cione et al., 2013; Jaimes et al., 2015; Lee & Chen 2012; Shay et al., 2000), though none have quantitatively examined how those asymmetries influence the TKE distribution. Though not included in this study, the asymmetric distribution of turbulent properties in the surface layer is also influenced by the surface wave field because of how it may modify the drag coefficient and enthalpy fluxes, especially outside the eyewall region (e.g., S. S. Chen et al., 2007, 2013; Donelan et al., 2012, 2014).

It is worth noting that this section only focuses on storm-motion relative asymmetries because the simulated TCs in this study did not exhibit classical asymmetric structures of a mature TC relative to environmental

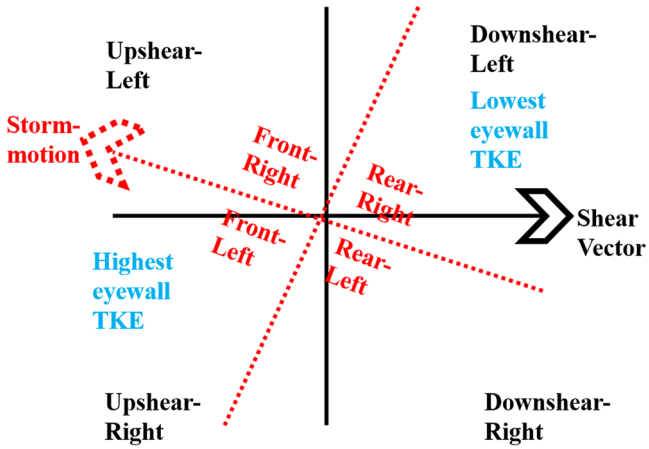

Figure 9. Schematic representation of the storm-motion relative and environmental wind shear relative coordinate systems used in this study. Areas with the highest and lowest turbulent kinetic energy are overlaid.

vertical wind shear such as a deeper inflow layer in the downshear quadrants (e.g., Reasor et al., 2013). This is likely because the vortices were either so intense that they are resilient to shear (CAT5 simulations), or the asymmetric distributions from the overlapping effects of wind shear and storm motion predominately resemble the effects of storm motion (CAT1 simulations). Nevertheless, the storm-motion relative and environmental shear relative coordinate systems largely overlap (Figure 9), with the storm-motion vector ~30° to the right of the upshear direction in all simulations.

To highlight the effect of TKE advection on the storm-relative location of the TKE maxima, plan views of the logarithm of TKE at 500, 1,000, and 2,000 m altitudes for the CAT5 simulations are presented in Figure 10. At all three altitudes of the CAT5-WA simulation (Figures 10a–10c), there is a distinct maximum of TKE in the front-left quadrant and a minimum of TKE in the rear-right quadrant. There is more asymmetry in the TKE distribution at 1,000-m and 2,000-m altitude than at 500-m altitude. In contrast to the distribution in the CAT5-WA simulation, the maximum TKE is in the direction of storm motion and the TKE minimum is closer to the rear of the vortex at all three altitudes of the CAT5-NA simulation (Figures 10d–10f).

At 500, 1,000, and 2,000 m altitudes of the front-left quadrant of the CAT5-WA simulation, the TKE maximum is located within a radial gradient of TKE advection (Figures 11a–11c) which is present because the axis of maximum TKE is radially inwards of the RMW (e.g., Figure 5e). The direction of the radial gradient reverses between 1,000 and 2,000-m altitude because the higher altitude is above the inflow layer (Figure 4a) and vertical advection likely plays a more dominant role there. At 500 and 1,000 m altitudes, the largest values of positive TKE advection are located within the front-left quadrant, just radially outward of the maximum of TKE. This relationship is also true at 2,000-m altitude, though the maximum value of positive TKE advection is radially inward of the maximum TKE values. Additionally, at all of these altitudes, the minimum of TKE in the rear-right quadrant is located near the lowest values of positive TKE advection. Thus, even though we cannot separate the vertical and horizontal TKE advection terms, it is clear that the inclusion of TKE advection influences the horizontal distribution of TKE such that both the TKE maximum and minimum are farther downwind than the simulations without TKE advection.

The plan views of the TKE in the CAT1 simulations (Figure 12) show a more extreme asymmetry than in the CAT5 simulations. In both CAT1 simulations, the majority of TKE at 500 and 1,000 m altitudes is confined to the quadrants ahead of storm motion. The higher magnitudes of the logarithm of TKE in the CAT1-WA can be attributed to the higher wind speeds. Though not as pronounced, the effect of TKE advection on the horizontal distribution of TKE in the CAT1 simulations at these altitudes is very similar to that in the CAT5 simulations. At both 500 and 1,000-m altitude, the CAT1-WA simulation has a TKE maxima in the front-left quadrant, while the CAT1-NA simulation has a TKE maxima farther upwind and closer to the direction of storm motion. Interestingly, the TKE maximum is farther downwind at 500-m altitude in the CAT1-WA simulation than in the CAT1-NA simulation, even though the majority of the domain at this altitude is in the inflow layer (Figure 4c) and characterized by negative TKE advection (Figure 11d). The majority of the domain at both 1,000 and 2,000-m altitude is characterized by positive TKE advection (Figures 11e and 11f) because that is above the inflow layer. At these altitudes, the maximum TKE values are co-located with a maximum of positive TKE advection.

The asymmetric distribution of TKE in the low-levels of the eyewall is reaffirmed in all simulations (Figure 13) using the same radial bins as Figure 8. To control for how the TKE values are related to wind speed, the TKE in each quadrant of Figure 13 was normalized by the square of the azimuthally averaged wind speed at 2-km altitude of that simulation. In both CAT5 simulations, the height of maximum eyewall TKE occurs at the highest altitude in the front-left quadrant and the lowest altitude in the rear-right quadrant. The height of maximum TKE in the rear-right quadrant is ~400 m, while it is ~1,000 m in the front-left quadrant. Similar to the axisymmetric results in Figure 4, the inclusion of TKE advection does not significantly affect the height of maximum TKE, except in the rear-left (RL) quadrant where the advection of TKE downwind from the region of maximum TKE increases the amount of TKE and the altitude of maximum TKE. Additionally, since there are similar maximum values of normalized TKE in the front-left quadrant, the differences in the actual TKE output values between the

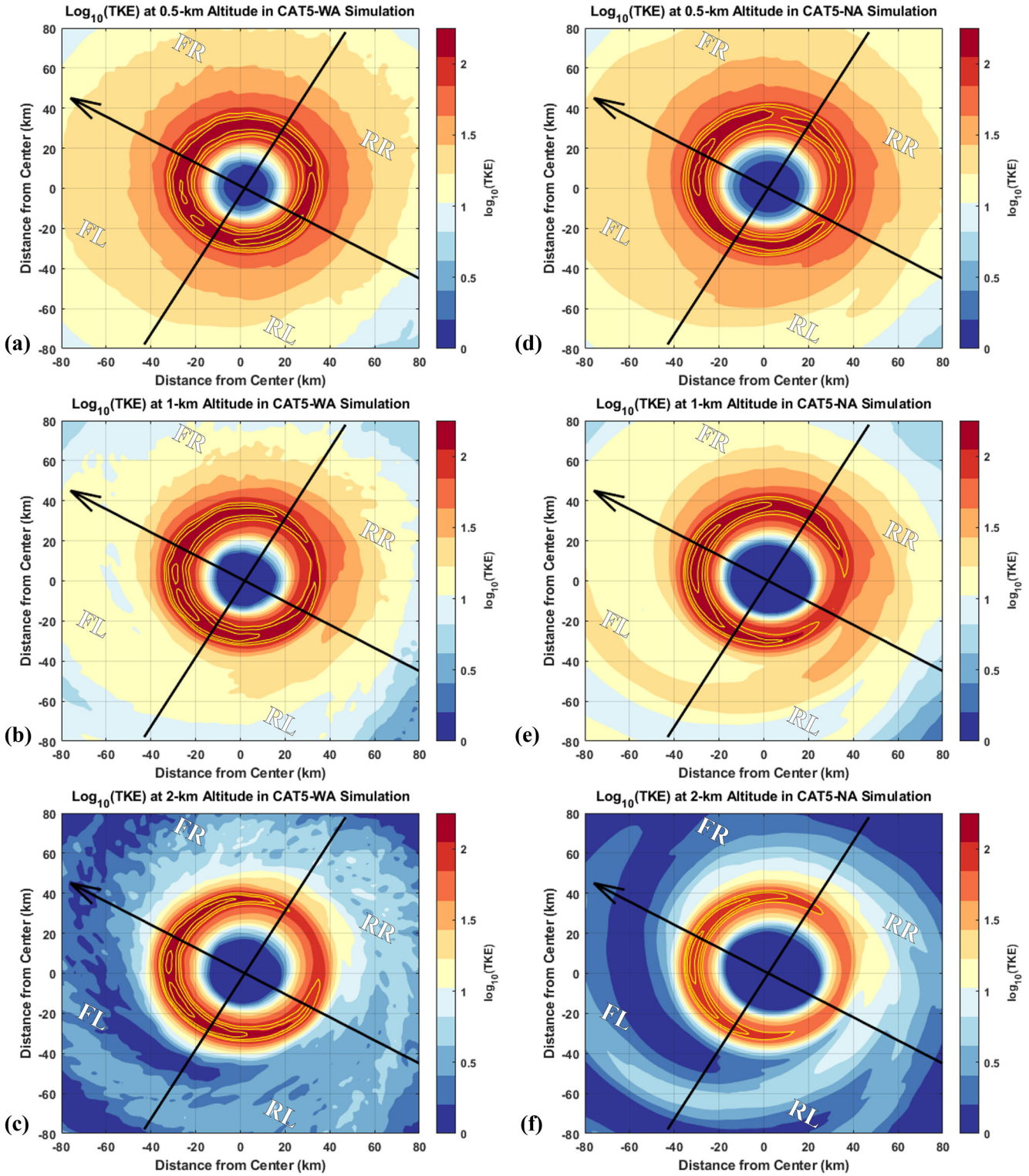

Figure 10. Log_{10}(TKE) in storm-motion relative quadrants (shaded) in the CAT5-WA simulation at (a) 500 m, (b) 1,000 m, and (c) 2,000 m, averaged over the last 24 hr of the simulations; (d), (e), and (f), as in (a), (b), (c), but for the CAT5-NA simulation. Values of 90%, 93%, 96%, and 99% the peak TKE values are contoured in yellow to further highlight regions of maximum TKE within the eyewall. The storm motion (arrow) along with the front-right (FR), front-left (FL), rear-right (RR), and rear-left (RL) are indicated.

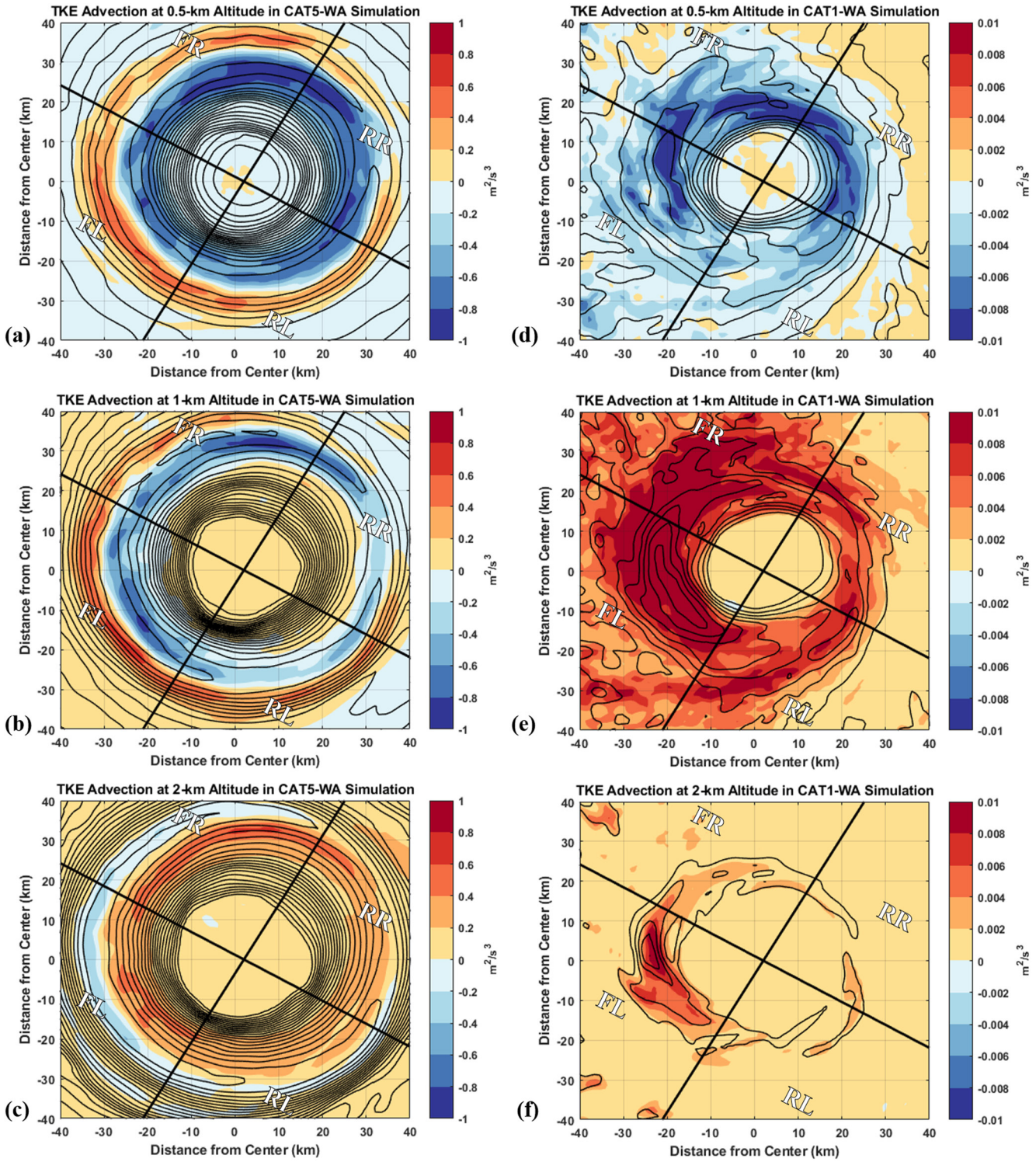

Figure 11. Plan view of turbulent kinetic energy (TKE) advection (shaded) and Log_{10}(TKE) (contoured) in storm-motion relative quadrants in the CAT5-WA simulation at (a) 500 m, (b) 1,000 m, and (c) 2,000 m, averaged over the last 24 hr of the simulations; (d), (e), and (f), as in (a), (b), (c), but for the CAT1-WA simulation. The front-right (FR), front-left (FL), rear-right (RR), and rear-left (RL) are indicated.

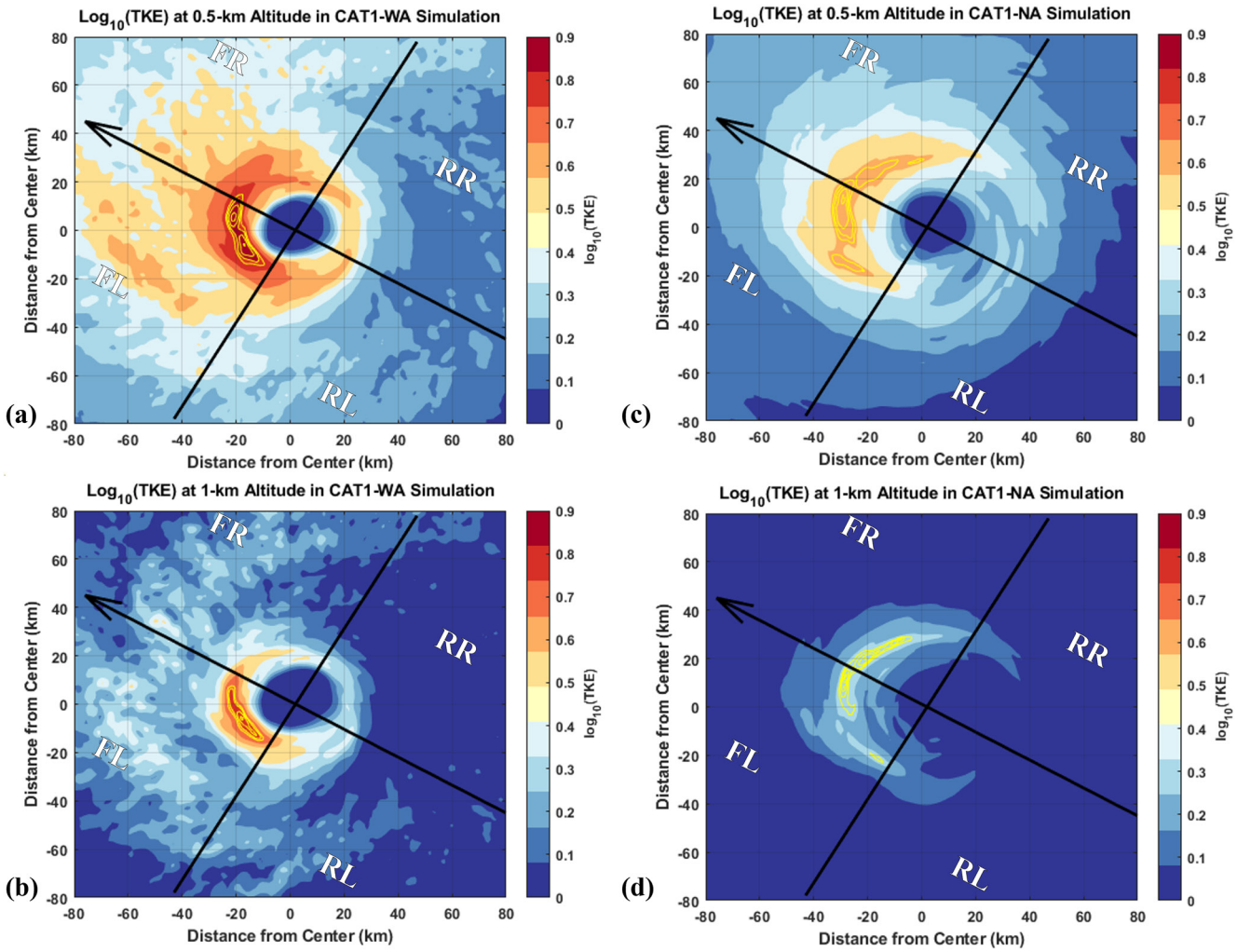

Figure 12. Log_{10}(TKE) in storm-motion relative quadrants in the CAT1-WA simulation at (a) 500 m and (b) 1,000 m, averaged over the last 24 hr of the simulation; (c), (d), as in (a), (b) but for the CAT1-NA simulation. Values of 90%, 93%, 96%, and 99% the peak TKE values are contoured in yellow to further highlight regions of maximum TKE within the eyewall. The storm motion (arrow) along with the front-right (FR), front-left (FL), rear-right (RR), and rear-left (RL) are indicated.

simulations can be attributed to the intensity differences between the simulations rather than to a redistribution by advection. The reasons why TKE advection produces a stronger vortex is discussed by X. Chen and Bryan (2021) and is generally attributed to a larger inflow angle, stronger inflow near the RMW, and stronger maximum diabatic heating radially inward of the RMW.

Similar maximum values of normalized TKE values also appear between the CAT1 simulations, though the front-right (FR) quadrant has the highest normalized TKE values in the CAT1-NA simulation while the front-left quadrant has the highest normalized TKE values in the CAT1-WA simulation. The difference in the height of maximum TKE between quadrants with the highest and lowest values is only ~100 m in the CAT1 simulations. As shown for the axisymmetric fields, TKE decreases more quickly with height in the simulations without advection in every quadrant than the simulations with advection.

While the inclusion of TKE advection leads to both a TKE maxima and minima that is farther downwind, the general wavenumber-1 asymmetry of low TKE in the rear-right quadrant and high TKE in the front-left quadrant is present in all the simulations and is related to the effects of storm motion and SST cooling. The SST outside of the RMW is ~0.5°C cooler in the rear of the storm (lowest in the rear-right quadrant), than on the front side of the TC (Figures 14a and 14c; simulations without TKE advection not shown but are similar). The differences in SSTs lead to asymmetries in and air-sea enthalpy fluxes by ~300 W m^{-2} (15% difference) in the eyewall of the CAT5-WA simulation (Figure 14b) and by ~40 W m^{-2} (28% difference) in the eyewall of the CAT1-WA simulation

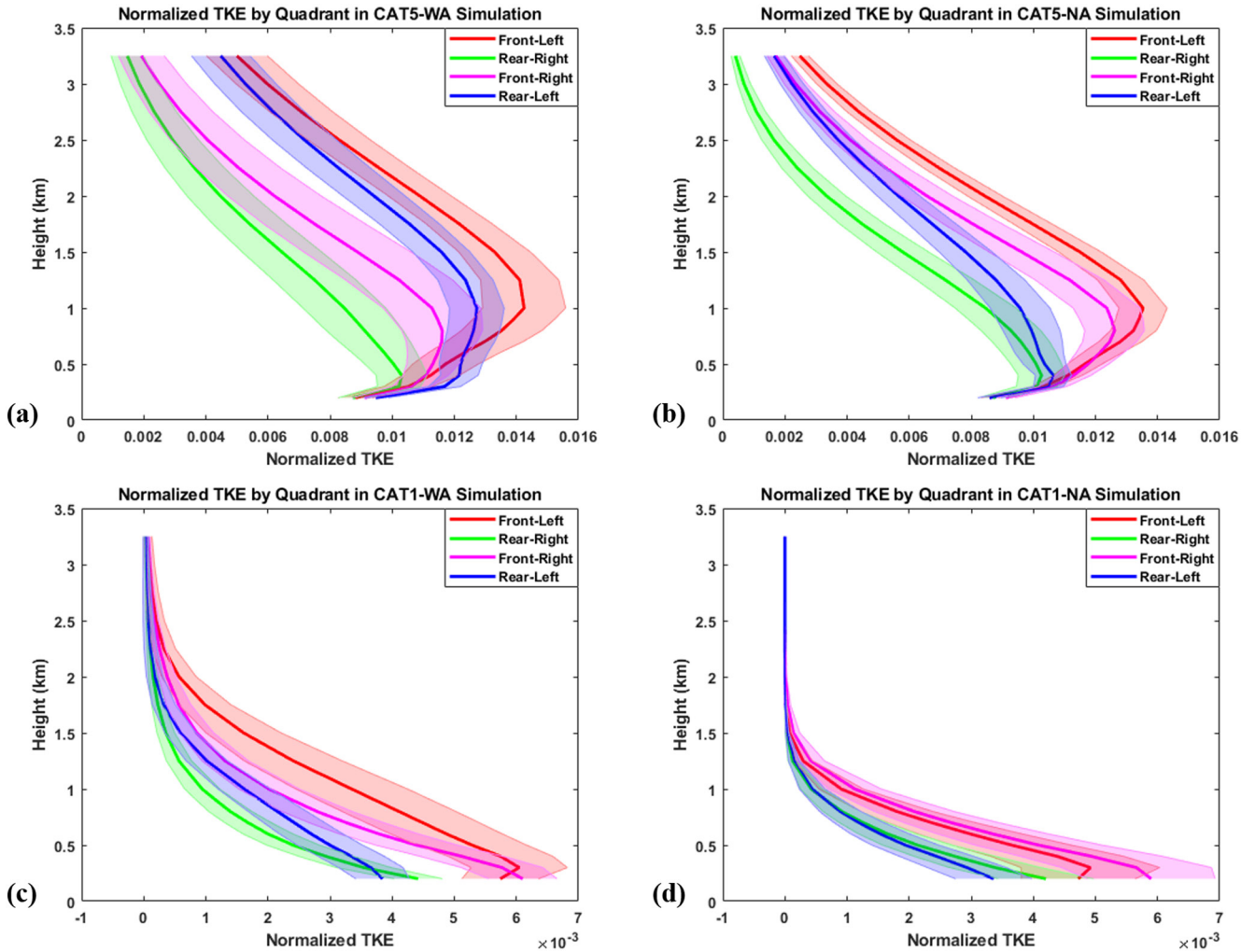

Figure 13. Eyewall turbulent kinetic energy normalized by the square of the mean wind speed at the 2-km radius of maximum winds (RMW) in storm-motion relative quadrants in the (a) CAT5-WA, (b) CAT5-NA, (c) CAT1-WA, (d) CAT1-NA simulations, averaged over the last 24 hr of the simulations. The terms are centered on the 500 m RMW in each simulation and averaged 5 km radially inward and outward.

(Figure 14d). The asymmetric distribution in enthalpy fluxes directly leads to asymmetric distribution of stability profiles (Figures 15a and 15c). At 300-m altitude of the CAT5-WA simulation, the largest virtual potential temperature gradient within 100 km of the storm center is in the rear-right quadrant (most stable), while the smallest gradient is in the front-left quadrant (least stable). The differences between the quadrants decrease with height and become minimal above 500 m altitude (not shown). At 300 m altitude of the CAT1-WA simulation (Figure 15c), the RL quadrant is the most stable in the eyewall region. However, at larger radii, both the FR and rear-right quadrants are the most stable. Above 300-m altitude, the differences between the quadrants become minimal (not shown).

Besides variations in stability, another dominant mechanism for the asymmetric distribution of TKE in all simulations, regardless of the inclusion of TKE advection, is the variations in wind stress due to storm motion and an asymmetric wind field. In the CAT5-WA simulation (Figure 15b), the wind stress in the right-of-motion quadrants is greater than the left-of-motion quadrants by ∼0.4 N m^{-2} (3% difference). In the CAT1-WA simulation (Figure 15d), the FR quadrant also has the largest wind stress, followed by the rear-right quadrant (difference of ∼0.2 N m^{-2}). In the CAT1-WA simulation, there is also a greater asymmetry between the quadrants as the FR quadrant has a larger wind stress than in the RL quadrant (smallest wind stress) by ∼0.8 N m^{-2} (44% difference). The simulations without TKE advection have similar relationships in wind stress between quadrants (not shown). The enhanced wind stress on the right of the storm may be obscuring the asymmetries in TKE due to differences in enthalpy fluxes and atmospheric stability. Though a

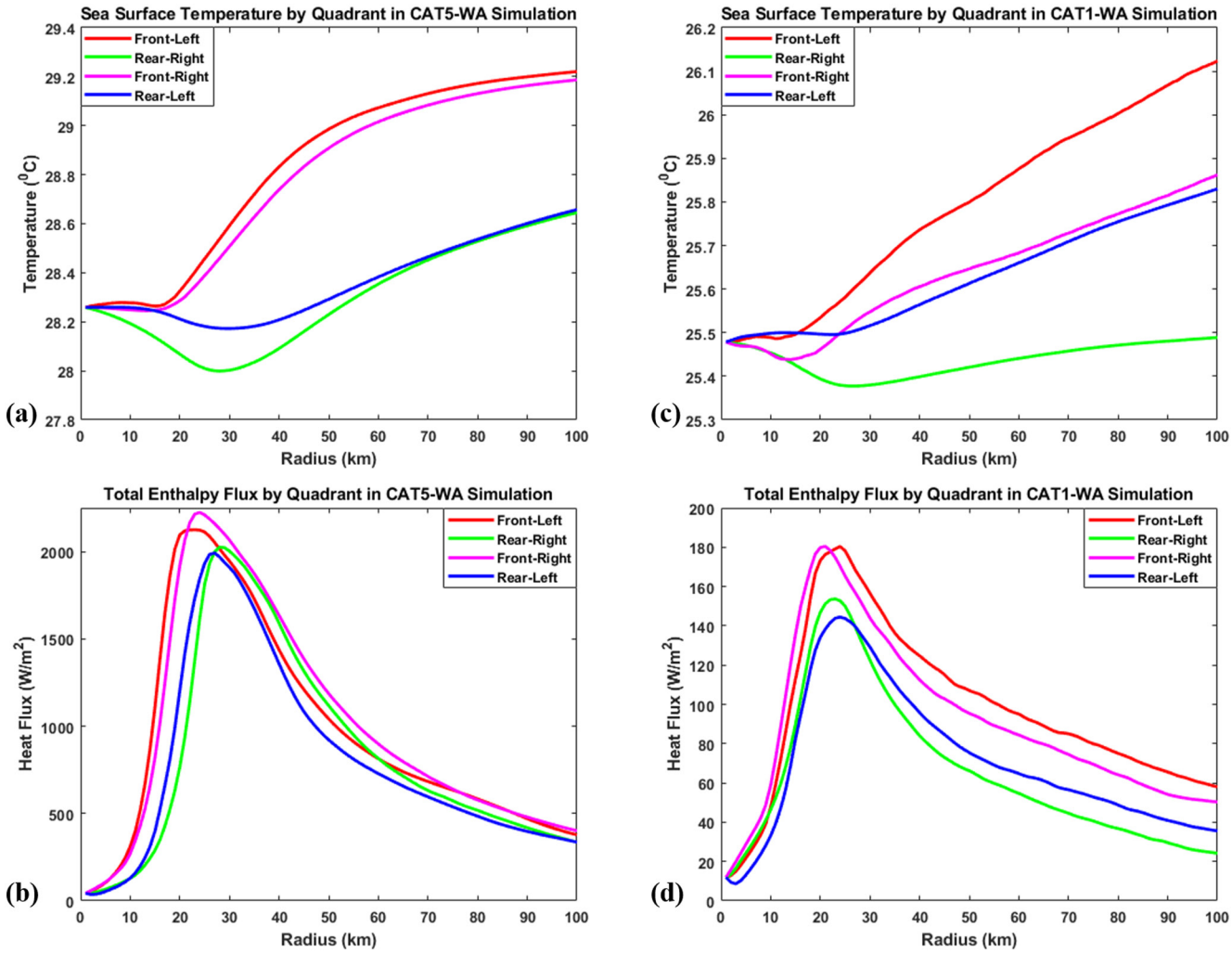

Figure 14. Storm-motion relative (a) sea surface temperature and (b) total enthalpy flux, averaged over the last 24 hr of the simulations of the CAT5-WA simulation; (c), (d), as in (a), and (b), but for the CAT1-WA simulation.

wind-wave model was not part of the simulations in this manuscript, the asymmetric distribution wind stress (and hence TKE) could be changed by surface ocean waves which can vary the surface roughness and the drag coefficient.

With the consistent TKE generation/destruction mechanisms in the FR and RL quadrants of all simulations, the redistribution of TKE due to advection plays a role in determining the quadrant with the second highest or lowest TKE magnitudes. Above 500-m altitude of the CAT5-WA simulation, the second lowest quadrant-averaged eyewall TKE magnitude is in the FR quadrant (Figure 13a). At 500 and 1,000-m altitude, the eyewall in the FR quadrant contains the largest negative contribution of TKE advection (Figures 11a and 11b). The low TKE magnitudes from the rear-right quadrant of the CAT5-NA simulation cannot be advected into the FR quadrant. Thus, in the CAT5-NA simulation, the RL quadrant has the second lowest TKE values (Figure 13b).

In both CAT1 simulations, the second lowest quadrant-averaged eyewall TKE magnitudes are located in the RL quadrant (Figures 13c and 13d). At 500 m altitude in the CAT1-WA simulation, the greatest reduction of TKE due to advection is in the quadrants ahead of storm motion (Figure 11d). In the CAT1-WA simulation, the mean winds are likely too weak to advect the low TKE magnitudes from the rear-right quadrant to the FR quadrant before the parcels become convectively unstable due to higher air-sea enthalpy fluxes and surface wind stress. Thus, TKE advection does not affect the asymmetric distribution of TKE in the eyewall as significantly in the CAT1-WA simulation as in the CAT5-WA simulation.

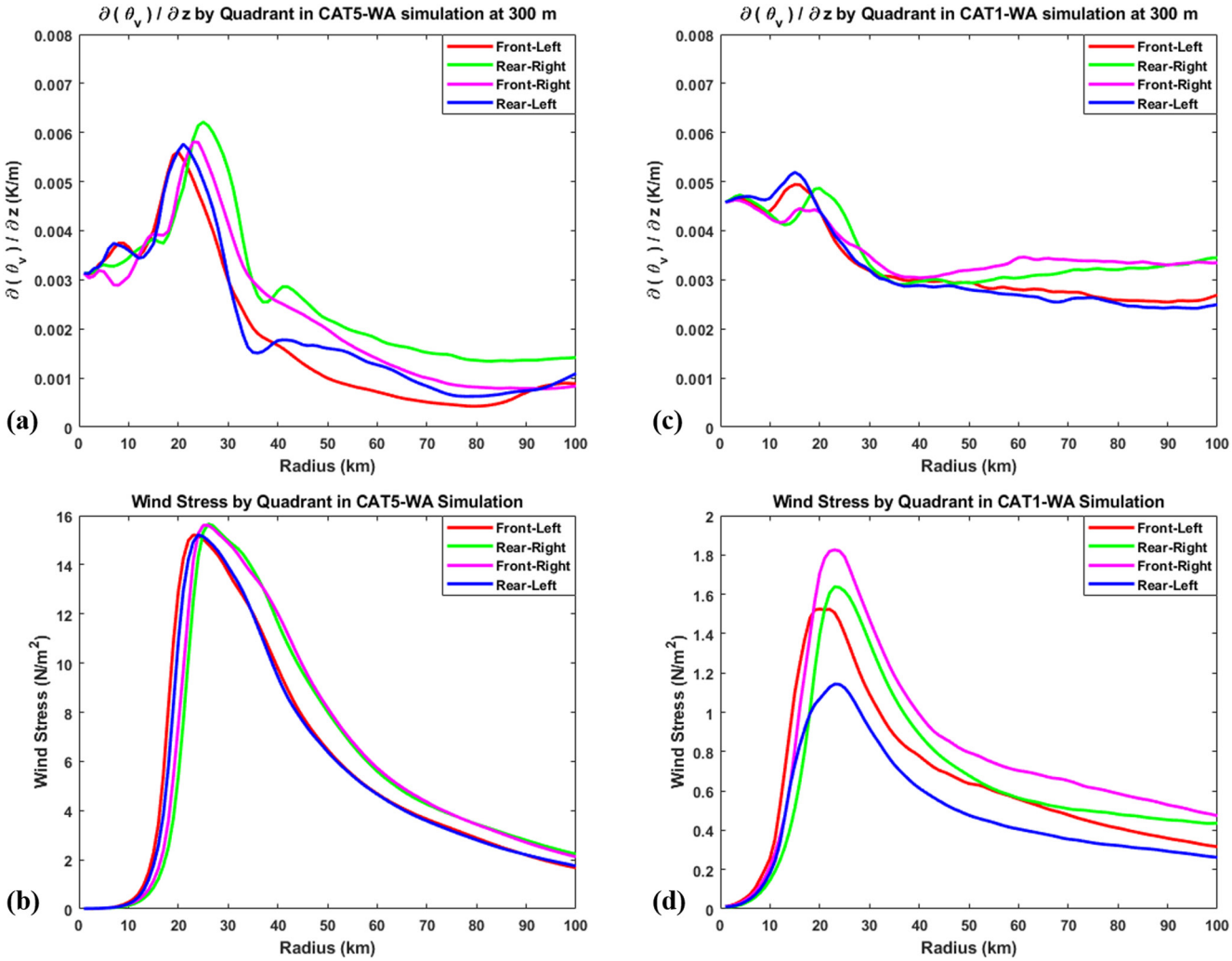

Figure 15. (a) vertical gradient of virtual potential temperature in storm-motion relative quadrants at 300-m altitude and (b) surface wind stress of the CAT5-WA simulation, averaged over the last 24 hr of the simulations. (c), (d) as in (a), (b), but for the CAT1-WA simulation.

4. Discussion and Conclusion

Idealized TCs subject to environmental wind shear and oceanic coupling are used to estimate the spatial characteristics of TKE and its budget terms in relation to TC structure and intensity. Similar to a recent study by X. Chen and Bryan (2021), the vortices are simulated with TKE advection turned on or off. Simulations are performed for three ocean regimes which vary the air-sea enthalpy fluxes, produce realistic SST cooling, and lead to simulated intensities ranging from category-1 to category-5 hurricane. This study builds upon the results of X. Chen and Bryan (2021) by using idealized TCs with environmental flow and oceanic coupling to examine how the inclusion of TKE advection influences the three-dimensional distribution of TKE and its budget terms.

The axisymmetric distribution of TKE, averaged over the last 24 hr of each simulation, is described as a function of height and radius. While the model-produced TKE agrees well with estimates from flight-level data shown in Zhang et al. (2011) and with estimates derived from the Coyote UAS over a wide-range of wind speeds, direct observations of turbulence at high wind speeds in the hurricane boundary layer are unavailable. Therefore, the results represent a model-based estimate of how the TKE distribution is related to storm structure over a wide range of wind speeds.

In all simulations, when the TKE was normalized by its maximum value to account for differences in intensity, the maximum TKE values were located ~0.5 km radially inward of the 1-km altitude RMW and near the base of eyewall updrafts. The maximum TKE was at ~1-km altitude in the CAT5 simulations while it was at

~300-m altitude in the CAT1 simulations. Above the TKE maximum, the TKE decays with height, but at a much larger rate for simulations without TKE advection. The results from analyzing the axisymmetric TKE distribution complement those of X. Chen and Bryan (2021), but using a different model, finer grid spacing, and different environmental conditions. These results highlight the need for boundary layer turbulence closure schemes to include TKE advection, since the simulations with TKE advection turned on qualitatively compare better to Doppler radar derived estimates of TKE (Lorsolo et al., 2010) than the simulations with TKE advection turned off.

The axisymmetric TKE budget terms also exhibit some interesting characteristics. At the base of the eyewall, the magnitude of the shear production term exceeds dissipation in the CAT5 simulations, while the two terms generally cancel each other in the CAT1 simulations. In all simulations, the vertical turbulent transport tendency is negative and the buoyancy term is negligible at the base of the eyewall (i.e., <400 m). In the inflow layer, TKE advection negatively contributed to the TKE tendency because advection brings lower values of TKE from larger radii to the eyewall. Together, there is positive TKE change near the surface that decreased to zero by ~1,500-m altitude in the CAT5 simulations and ~500-m altitude in the CAT1 simulations. The decrease of TKE change with height is dependent on all of the TKE budget terms since shear production and dissipation (the two largest terms) largely cancel each other. Even though the magnitude of the TKE budget terms decrease with radius, all of the terms maintain the same general relationships to each other.

The TKE and its budget terms are also considered for different quadrants related to storm motion. At 500, 1,000, and 2,000 m altitude, the maximum TKE in simulations with TKE advection turned on occurs farther downwind in the front-left quadrant than simulations without TKE advection where the maximum TKE was closer to the direction of storm motion. The degree of TKE asymmetry increased with increasing altitude. For the CAT5 simulation with TKE advection turned on, the maximum values of TKE in the front-left quadrant were in a radial gradient of TKE advection. The maximum values of positive TKE advection occurred at a similar azimuth as the maximum TKE values. The maximum TKE values and maximum positive TKE advection are not co-located because the axis of maximum TKE is radially inwards of the RMW.

Mechanisms for TKE generation were also explored, regardless of the inclusion of TKE advection. In quadrant-averages, the maximum TKE magnitude and height of the maximum TKE are consistently the largest in the front-left quadrant (highest SSTs and enthalpy fluxes) and lowest in the rear-right quadrant (lowest SSTs and enthalpy fluxes). In all simulations, higher enthalpy fluxes in the front-left quadrant were associated with a more statically unstable boundary layer while lower enthalpy fluxes in the rear-right quadrant were associated with a more statically stable boundary layer. The wavenumber-1 asymmetry in boundary layer TKE may be partially offset by a maximum in wind stress on the right side of the storm. The exact mechanisms for the asymmetric TKE distribution are a topic of future work.

This study provides a model-produced estimate of the time-averaged storm-scale spatial distribution of TKE and its budget terms, and how those distributions were related to the inclusion of TKE advection. The results show that the inclusion of TKE advection leads to a more realistic model-produced distribution of TKE in the mid-to-upper levels of the eyewall and changes the horizontal location of maximum TKE values. The results also highlight the need for in situ measurements of turbulence in TCs, especially in the inflow layer and eyewall, to verify the accuracy of the simulated TKE distribution and to improve future parameterizations. Such measurements may be achieved with uncrewed aircraft and will provide valuable insights to help design and implement boundary layer parameterizations and improve TC intensity forecasts. Further measurements through remote sensing instruments such as the IWRAP used in Sroka and Guimond (2021) and synthetic aperture radar can also be very valuable to advance our understanding of TKE distributions. A follow up study using a LES would be useful since that modeling framework can explicitly resolve more spatial scales. The understanding of the TKE production associated with time dependent features in the TC such as the eyewall mesovortices, rainbands, and convective cells over the open ocean can also be explored with numerical simulations similar to those in this study, or with a LES. Future work should also use higher resolution simulations to consider 3-D contributions of the TKE equation to the TKE budget in order to render the model data more like a 3-D hurricane. It is likely that the distribution of the TKE budget terms in numerical simulations are sensitive to the choice of boundary layer parameterization scheme which have varying degrees of turbulent mixing (Kepert 2012; Zhu et al., 2014). Testing the distribution among the terms for other boundary layer parameterizations is a topic of future work.

Data Availability Statement

All the data used in this manuscript in NETCDF format with a README file describing the variables is available at the Embry-Riddle Aeronautical University Scholarly Commons Repository at: https://commons.erau.edu/dm-advection-turbulent-kinetic-energy/. The WRF model is available for download at https://github.com/wrf-model/WRF.

Acknowledgments
This research was carried out [in part] under the auspices of the Cooperative Institute for Marine and Atmospheric Studies (CIMAS), a Cooperative Institute of the University of Miami and the National Oceanic and Atmospheric Administration, cooperative agreement NA20OAR4320472. Computational time was generously provided by the Center for Computational Sciences at the University of Miami. The authors are appreciative for NCAR-MMM making the WRF model freely available and the comments from two anonymous reviewers which greatly helped to improve the manuscript. We also appreciate program support from the NOAA Office of Marine and Aviation Operations, Uncrewed Systems Operations Center 2021 Request for Proposals. Jun Zhang is supported by NOAA Grants NA21OAR4590370, NA22OAR4590178, and NA22OAR4050669D. David Nolan was supported by NSF Grant ICER-1663947.

References

Beljaars, A. C. M. (1994). The parameterization of surface fluxes in large-scale models under free convection. *Quarterly Journal of the Royal Meteorological Society*, *121*(522), 255–270. https://doi.org/10.1002/qj.49712152203

Bell, M. M., Montgomery, M. T., & Emanuel, K. A. (2012). Air–sea enthalpy and momentum exchange at major hurricane wind speeds observed during CBLAST. *Journal of the Atmospheric Sciences*, *69*(11), 3197–3222. https://doi.org/10.1175/JAS-D-11-0276.1

Black, M., Gamache, J., Marks, F., Samsury, C., & Willoughby, H. (2002). Eastern Pacific Hurricanes Jimena of 1991 and Olivia of 1994: The effect of vertical shear on structure and intensity. *Monthly Weather Review*, *130*(9), 2291–2312. https://doi.org/10.1175/1520-0493(2002)130<2291:ephjoa>2.0.co;2

Black, P. G. (1983). *Ocean temperature changes induced by tropical cyclones* Ph.D. dissertation. (p. 278). The Pennsylvania State University.

Black, P. G., D'Asaro, E. A., Drennan, W. M., French, J. R., Niiler, P. P., Sanford, T. B., et al. (2007). Air–sea exchange in hurricanes: Synthesis of observations from the coupled boundary layer air–sea transfer experiment. *Bulletin America Meteorology Social*, *88*(3), 357–374. https://doi.org/10.1175/bams-88-3-357

Braun, S. A., Sippel, J. A., & Nolan, D. S. (2012). The impact of dry midlevel air on hurricane intensity in idealized simulations with no mean flow. *Journal of the Atmospheric Sciences*, *69*(1), 236–257. https://doi.org/10.1175/JAS-D-10-05007.1

Braun, S. A., & Tao, W.-K. (2000). Sensitivity of high-resolution simulations of Hurricane Bob (1991) to planetary boundary layer parameterizations. *Monthly Weather Review*, *128*(12), 3941–3961. https://doi.org/10.1175/1520-0493(2000)129<3941:SOHRSO>2.0.CO;2

Bryan, G. H., & Fritsch, J. M. (2002). A benchmark simulation for moist nonhydrostatic numerical models. *Monthly Weather Review*, *130*(12), 2917–2928. https://doi.org/10.1175/1520-0493(2002)130<2917:absfmn>2.0.co;2

Chen, S. S., Price, J. F., Zhao, W., Donelan, M. A., & Walsh, E. J. (2007). The CBLAST- hurricane program and the next-generation fully coupled atmosphere-wave-ocean models for hurricane research and prediction. *Bulletin America Meteorology Social*, *88*(3), 311–317. https://doi.org/10.1175/bams-88-3-311

Chen, S. S., Zhao, W., Donelan, M. A., & Tolman, H. L. (2013). Directional wind-wave coupling in fully coupled atmosphere-wave-ocean models: Results from CBLAST-Hurricane. *Journal of the Atmospheric Sciences*, *70*(10), 3198–3215. https://doi.org/10.1175/jas-d-12-0157.1

Chen, X., & Bryan, G. H. (2021). Role of advection of parameterized turbulence kinetic energy in idealized tropical cyclone simulations. *Journal of the Atmospheric Sciences*. https://doi.org/10.1175/JAS-D-21-0088.1

Cione, J. J. (2015). The relative roles of the ocean and atmosphere as revealed by buoy air- sea observations in hurricanes. *Monthly Weather Review*, *143*(3), 904–913. https://doi.org/10.1175/MWR-D-13-00380.1

Cione, J. J., Bryan, G. H., Dobosy, R., Zhang, J. A., de Boer, G., Aksoy, A., et al. (2020). Eye of the storm: Observing hurricanes with a small unmanned aircraft system. *Bulletin America Meteorology Social*, *101*(2), E186–E205. https://doi.org/10.1175/BAMS-D-19-0169.1

Cione, J. J., Kalina, E. A., Zhang, J. A., & Uhlhorn, E. W. (2013). Observations of air–sea interaction and intensity change in hurricanes. *Monthly Weather Review*, *141*(7), 2368–2382. https://doi.org/10.1175/MWR-D-12-00070.1

Donelan, M. A. (1990). Air-sea interaction ocean engineering science. In B. Le Méhauté, & D. M. Hanes, (Eds.), *The sea: Ideas and observations on progress in the study of the seas* (Vol. 9, pp. 239–292). John Wiley and Sons.

Donelan, M. A., Curcic, M., Chen, S. S., & Magnusson, A. K. (2012). Modeling waves and wind stress. *Journal of Geophysical Research*, *117*(C11), C00J23. https://doi.org/10.1029/2011JC007787

Donelan, M. A., Haus, B. K., Reul, N., Plant, W. J., Stiassnie, M., Graber, H. C., et al. (2004). On the limiting aerodynamic roughness of the ocean in very strong winds. *Geophysical Research Letters*, *31*(18), L18306. https://doi.org/10.1029/2004GL019460

Drennan, W. M., Zhang, J. A., French, J. R., McCormick, C., & Black, P. G. (2007). Turbulent fluxes in the hurricane boundary layer. Part II: Latent heat flux. *Journal of the Atmospheric Sciences*, *64*(4), 1103–1115. https://doi.org/10.1175/jas3889.1

Dunion, J. P. (2011). Rewriting the climatology of the tropical North Atlantic and Caribbean Sea atmosphere. *Journal of Climate*, *24*(3), 893–908. https://doi.org/10.1175/2010jcli3496.1

Dyer, A. J., & Hicks, B. B. (1970). Flux–gradient relationships in the constant flux layer. *Quarterly Journal of the Royal Meteorological Society*, *96*(410), 715–721. https://doi.org/10.1002/qj.49709641012

Efstathiou, G. A., Beare, R. J., Osborne, S., & Lock, A. P. (2016). Grey zone simulations of the morning convective boundary layer development. *Journal of Geophysical Research: Atmospheres*, *121*(9), 4769–4782. https://doi.org/10.1002/2016JD024860

Emanuel, K. A. (1995). Sensitivity of tropical cyclones to surface exchange coefficients and a revised steady-state model incorporating eye dynamics. *Journal of the Atmospheric Sciences*, *52*(22), 3969–3976. https://doi.org/10.1175/1520-0469(1995)052<3969:sotcts>2.0.co;2

Finocchio, P. M., Majumdar, S. J., Nolan, D. S., & Iskandarani, M. (2016). Idealized tropical cyclone responses to the height and depth of environmental vertical wind shear. *Monthly Weather Review*, *144*(6), 2155–2175. https://doi.org/10.1175/MWR-D-15-0320.1

Foster, R. (2013). Signature of large aspect ratio roll vortices in synthetic aperture radar images of tropical cyclones. *Oceanography*, *26*, 58–67. http://www.jstor.org/stable/24862036

French, J. R., Drennan, W. M., Zhang, J. A., & Black, P. G. (2007). Turbulent fluxes in the hurricane boundary layer. Part I: Momentum flux. *Journal of the Atmospheric Sciences*, *64*(4), 1089–1102. https://doi.org/10.1175/jas3887.1

Gray, W. M. (1998). The formation of tropical cyclones. *Meteorology and Atmospheric Physics*, *67*(1–4), 37–69. https://doi.org/10.1007/bf01277501

Greatbatch, R. J. (1983). On the response of the ocean to a moving storm: The nonlinear dynamics. *Journal of Physical Oceanography*, *13*(3), 357–367. https://doi.org/10.1175/1520-0485(1983)013<0357:otroto>2.0.co;2

Green, B. W., & Zhang, F. (2014). Sensitivity of tropical cyclone simulations to parametric uncertainties in air–sea fluxes and implications for parameter estimation. *Monthly Weather Review*, *142*(6), 2290–2308. https://doi.org/10.1175/MWR-D-13-00208.1

Green, B. W., & Zhang, F. (2015). Idealized large-eddy simulations of a tropical cyclone–like boundary layer. *Journal of the Atmospheric Sciences*, *72*(5), 1743–1764. https://doi.org/10.1175/JAS-D-14-0244.1

Guimond, S. R., Sroka, S., & Proztko, D. (2018). A large eddy simulation of hurricane intensification. In *33rd conference on hurricanes and tropical meteorology* (p. 17). American Meteorological Society. Retrieved from https://ams.confex.com/ams/33HURRICANE/webprogram/Manuscript/Paper339570/larg%20e_eddy_33hurr_guimond.pdf

Guimond, S. R., Zhang, J. A., Sapp, J. W., & Frasier, S. J. (2018). Coherent turbulence in the boundary layer of Hurricane Rita (2005) during an eyewall replacement cycle. *Journal of the Atmospheric Sciences*, *75*(9), 3071–3093. https://doi.org/10.1175/jas-d-17-0347.1

Hogstrom, U. (1990). Analysis of turbulence structure in the surface layer with a modified similarity formulation for near neutral conditions. *Journal of the Atmospheric Sciences*, *47*(16), 1949–1972. https://doi.org/10.1175/1520-0469(1990)047<1949:aotsit>2.0.co;2

Hong, S. Y. (2010). A new stable boundary layer mixing scheme and its impact on the simulated East Asian summer monsoon. *Quarterly Journal of the Royal Meteorological Society*, *136*(651), 1481–1496. https://doi.org/10.1002/Qj.665

Hong, S.-Y., Dudhia, J., & Chen, S.-H. (2004). A revised approach to ice microphysical processes for the bulk parameterization of clouds and precipitation. *Monthly Weather Review*, *132*(1), 103–120. https://doi.org/10.1175/1520-0493(2004)132<0103:aratim>2.0.co;2

Hong, S. Y., Noh, Y., & Dudhia, J. (2006). A new vertical diffusion package with an explicit treatment of entrainment processes. *Monthly Weather Review*, *134*(9), 2318–2341. https://doi.org/10.1175/Mwr3199.1

Honnert, R., & Masson, V. (2014). What is the smallest physically acceptable scale for 1D turbulence schemes? *Frontiers in Earth Science*, *2*, https://doi.org/10.3389/feart.2014.00027

Jacob, S. D., Shay, L. K., Mariano, A. J., & Black, P. G. (2000). The 3D oceanic mixed layer response to Hurricane Gilbert. *Journal of Physical Oceanography*, *30*(6), 1407–1429. https://doi.org/10.1175/1520-0485(2000)030<1407:TOMLRT>2.0.CO;2

Jaimes, B., & Shay, L. K. (2009). Mixed layer cooling in mesoscale oceanic eddies during Hurricanes Katrina and Rita. *Monthly Weather Review*, *137*, 4188–4207. https://doi.org/10.1175/2009MWR2849.1

Jaimes, B., Shay, L. K., & Uhlhorn, E. W. (2015). Enthalpy and momentum fluxes during hurricane earl relative to underlying ocean features. *Monthly Weather Review*, *143*(1), 111–131. https://doi.org/10.1175/MWR-D-13-00277.1

Janjic, Z. I. (1990). The step-mountain coordinate: Physical package. *Monthly Weather Review*, *118*, 1429–1443.

Janjic, Z. I. (1994). The step-mountain Eta coordinate model: Further developments of the convection, viscous layer, and turbulence closure schemes. *Monthly Weather Review*, *122*, 927–945.

Jordan, C. L. (1958). Mean soundings for the West Indies area. *Journal of Meteorology*, *5*(1), 91–97. https://doi.org/10.1175/1520-0469(1958)015<0091:msftwi>2.0.co;2

Kain, J. S. (2004). The Kain–Fritsch convective parameterization: An update. *Journal of Applied Meteorology*, *43*(1), 170–181. https://doi.org/10.1175/1520-0450(2004)043<0170:tkcpau>2.0.co;2

Kaplan, J., & DeMaria, M. (2003). Large-scale characteristics of rapidly intensifying tropical cyclones in the North Atlantic basin. *Weather and Forecasting*, *18*(6), 1093–1108. https://doi.org/10.1175/1520-0434(2003)018<1093:lcorit>2.0.co;2

Katz, J., & Zhu, P. (2017). Evaluation of surface layer flux parameterization using in-situ observations. *Atmospheric Research*, *194*, 150–163. https://doi.org/10.1016/j.atmosres.2017.04.025

Kepert, J. D. (2006a). Observed boundary layer wind structure and balance in the hurricane core Part I: Hurricane Georges. *Journal of the Atmospheric Sciences*, *63*(9), 2169–2193. https://doi.org/10.1175/jas3745.1

Kepert, J. D. (2006b). Observed boundary layer wind structure and balance in the hurricane core Part II: Hurricane Mitch. *Journal of the Atmospheric Sciences*, *63*(9), 2194–2211. https://doi.org/10.1175/jas3746.1

Kepert, J. D. (2012). Choosing a boundary layer parameterization for tropical cyclone modeling. *Monthly Weather Review*, *140*(5), 1427–1445. https://doi.org/10.1175/MWR-D-11-00217.1

Lee, C., & Chen, S. S. (2012). Symmetric and asymmetric structures of hurricane boundary layer in coupled atmosphere–Wave–ocean models and observations. *Journal of the Atmospheric Sciences*, *69*, 3576–3594. https://doi.org/10.1175/JAS-D-12-046.1

Lee, C.-Y., & Chen, S. S. (2014). Stable boundary layer and its impact on tropical cyclone structure in a coupled atmosphere-ocean model. *Monthly Weather Review*, *142*(5), 1927–1944. https://doi.org/10.1175/mwr-d-13-00122.1

Lenshow, D. H. (1970). Airplane measurements of planetary boundary layer structure. *Journal of Applied Meteorology*, *9*, 874–884.

Lorsolo, S., Schroeder, J. L., Dodge, P., & Marks, F. (2008). An observational study of hurricane boundary layer small-scale coherent structures. *Monthly Weather Review*, *136*, 2871–2893. https://doi.org/10.1175/2008MWR2273.1

Lorsolo, S., Zhang, J. A., Marks, F., & Gamache, J. (2010). Estimation and mapping of hurricane turbulent energy using airborne Doppler measurements. *Monthly Weather Review*, *138*(9), 3656–3670. https://doi.org/10.1175/2010MWR3183.1

Marks, F. D., Black, P. G., Montgomery, M. T., & Burpee, R. W. (2008). Structure of the eye and eyewall of Hurricane Hugo (1989). *Monthly Weather Review*, *136*(4), 1237–1259. https://doi.org/10.1175/2007mwr2073.1

Ming, J., & Zhang, J. A. (2016). Effects of surface flux parameterization on the numerically simulated intensity and structure of Typhoon Morakot (2009). *Advances in Atmospheric Sciences*, *33*(1), 58–72. https://doi.org/10.1007/s00376-015-4202-z

Montgomery, M. T., Smith, R. K., & Nguyen, S. V. (2010). Sensitivity of tropical cyclone models to the surface exchange coefficients. *Quarterly Journal of the Royal Meteorological Society*, *136*(653), 1945–1953. https://doi.org/10.1002/qj.702

Moss, M. S. (1978). Low-level turbulence structure in the vicinity of a hurricane. *Monthly Weather Review*, *106*(6), 841–849. https://doi.org/10.1175/1520-0493(1978)106<0841:lltsit>2.0.co;2

Moss, M. S., & Merceret, F. J. (1976). A note on several low-layer features of Hurricane Eloise (1975). *Monthly Weather Review*, *104*(7), 967–971. https://doi.org/10.1175/1520-0493(1976)104<0967:anosll>2.0.co;2

Moss, M. S., & Merceret, F. J. (1977). A comparison of velocity spectra from hot film anemometer and gust-probe measurements. *Journal of Applied Meteorology*, *16*(3), 319–320. https://doi.org/10.1175/1520-0450(1977)016<0319:acovsf>2.0.co;2

Nakanishi, M., & Niino, H. (2006). An improved Mellor–Yamada level 3 model: Its numerical stability and application to a regional prediction of advecting fog. *Boundary-Layer Meteorology*, *119*(2), 397–407. https://doi.org/10.1007/s10546-005-9030-8

Nakanishi, M., & Niino, H. (2009). Development of an improved turbulence closure model for the atmospheric boundary layer. *Journal of the Meteorological Society of Japan. Series II*, *87*(5), 895–912. https://doi.org/10.2151/jmsj.87.895

Nicholls, S., & Readings, C. J. (1985). Aircraft observations of the Ekman layer during the joint air-sea interaction experiment. *Quarterly Journal of the Royal Meteorological Society*, *105*(446), 785–802. https://doi.org/10.1002/qj.49710544604

Nolan, D. S. (2011). Evaluating environmental favorableness for tropical cyclone development with the method of point-downscaling. *Journal of Advances in Modeling Earth Systems*, *3*(8), M08001. https://doi.org/10.1029/2011MS000063

Nolan, D. S., Zhang, J. A., & Stern, D. P. (2009a). Evaluation of planetary boundary layer parameterizations in tropical cyclones by comparison of in situ observations and high-resolution simulations of Hurricane Isabel (2003). Part I: Initialization, maximum winds, and the outer-core boundary layer. *Monthly Weather Review*, *137*(11), 3651–3674. https://doi.org/10.1175/2009MWR2785.1

Nolan, D. S., Zhang, J. A., & Stern, D. P. (2009b). Evaluation of planetary boundary layer parameterizations in tropical cyclones by comparison of in situ observations and high-resolution simulations of Hurricane Isabel (2003). Part II: Inner-core boundary layer and eyewall structure. *Monthly Weather Review*, *137*(11), 3675–3698. https://doi.org/10.1175/2009mwr2786.1

Olson, J. B., Kenyon, J. S., Angevine, W. M., Brown, J. M., Pagowski, M., & Sušelj, K. (2019). A description of the MYNN-EDMF scheme and coupling to other components in WRF-ARW. In *NOAA technical memorandum* (Vol. 61, p. 37). OAR GSD. https://doi.org/10.25923/n9wm-be49

Onderlinde, M. J., & Nolan, D. S. (2014). Environmental helicity and its effects on development and intensification of tropical cyclones. *Journal of the Atmospheric Sciences*, *71*(11), 4308–4320. https://doi.org/10.1175/JAS-D-14-0085.1

Onderlinde, M. J., & Nolan, D. S. (2016). Tropical cyclone–relative environmental helicity and the pathways to intensification in shear. *Journal of the Atmospheric Sciences*, *73*(2), 869–890. https://doi.org/10.1175/JAS-D-15-0261.1

Paulson, C. A. (1970). The mathematical representation of wind speed and temperature profiles in the unstable atmospheric surface layer. *Journal of Applied Meteorology*, *9*(6), 857–861. https://doi.org/10.1175/1520-0450(1970)009<0857:tmrows>2.0.co;2

Powell, M. D., Vickery, P. J., & Reinhold, T. A. (2003). Reduced drag coefficient for high wind speeds in tropical cyclones. *Nature*, *422*(6929), 279–283. https://doi.org/10.1038/nature01481

Price, J. F. (1981). Upper ocean response to a hurricane. *Journal of Physical Oceanography*, *11*(2), 153–175. https://doi.org/10.1175/1520-0485(1981)011<0153:uortah>2.0.co;2

Price, J. F., Sanford, T. B., & Forristall, G. Z. (1994). Forced stage response to a moving hurricane. *Journal of Physical Oceanography*, *24*(2), 233–260. https://doi.org/10.1175/1520-0485(1994)024<0233:fsrtam>2.0.co;2

Reasor, P. D., Rogers, R. F., & Lorsolo, S. (2013). Environmental flow impacts on tropical cyclone structure diagnosed from airborne Doppler radar composites. *Monthly Weather Review*, *141*(9), 2949–2969. https://doi.org/10.1175/MWR-D-12-00334.1

Rios-Berrios, R., Davis, C. A., & Torn, R. D. (2018). A hypothesis for the intensification of tropical cyclones under moderate vertical wind shear. *Journal of the Atmospheric Sciences*, *75*(12), 4149–4173. https://doi.org/10.1175/jas-d-18-0070.1

Rogers, R., Reasor, P., & Lorsolo, S. (2013). Airborne Doppler observations of the inner-core structural differences between intensifying and steady-state tropical cyclones. *Monthly Weather Review*, *141*, 2970–2991. https://doi.org/10.1175/MWR-D-12-00357.1

Rotunno, R., Chen, Y., Wang, W., Davis, C., Dudhia, J., & Holland, G. J. (2009). Large-eddy simulation of an idealized tropical cyclones. *Bulletin America Meteorology Social*, *90*(12), 1783–1788. https://doi.org/10.1175/2009BAMS2884.1

Shay, L. K., Goni, G. J., & Black, P. G. (2000). Effects of a warm oceanic feature on Hurricane Opal. *Monthly Weather Review*, *128*(5), 1366–1383. https://doi.org/10.1175/1520-0493(2000)128<1366:EOAWOF>2.0.CO;2

Skamarock, W. C., Klemp, J. B., Dudhia, J., Gill, D. O., Barker, D., Duda, M. G., et al. (2008). A description of the advanced research WRF version 3. NCAR Technical Note NCAR/TN-4751STR. 125. http://www2.mmm.ucar.edu/wrf/users/docs/arw_v3.pdf

Smith, R. K., & Thomsen, G. L. (2010). Dependence of tropical-cyclone intensification on the boundary layer representation in a numerical model. *Quarterly Journal of the Royal Meteorological Society*, *136*(652), 1671–1685. https://doi.org/10.1002/qj.687

Sroka, S., & Guimond, S. R. (2021). Organized kinetic energy backscatter in the hurricane boundary layer from radar measurements. *Journal of Fluid Mechanics*, *924*, A21. https://doi.org/10.1017/jfm.2021.632

Tang, B., & Emanuel, K. (2010). Midlevel ventilation's constraint on tropical cyclone intensity. *Journal of the Atmospheric Sciences*, *67*(6), 1817–1830. https://doi.org/10.1175/2010jas3318.1

Tang, B., & Emanuel, K. (2012). A ventilation index for tropical cyclones. *Bulletin America Meteorology Social*, *93*(12), 1901–1912. https://doi.org/10.1175/bams-d-11-00165.1

Wadler, J. B., Rogers, R. F., & Reasor, P. D. (2018). The relationship between spatial variations in the structure of convective bursts and tropical cyclone intensification as determined by airborne Doppler radar. *Monthly Weather Review*, *146*(3), 761–780. https://doi.org/10.1175/MWR-D-17-0213.1

Wyngaard, J. C. (2004). Toward numerical modeling in the "Terra incognita". *Journal of the Atmospheric Sciences*, *61*(14), 1816–1826. https://doi.org/10.1175/1520-0469(2004)061<1816:tnmitt>2.0.co;2

Zhang, J. A., Rogers, R., Reasor, P., Uhlhorn, E., & Marks, F. (2013). Asymmetric hurricane boundary layer structure from dropsonde composites in relation to the environmental vertical wind shear. *Monthly Weather Review*, *141*(11), 3968–3984. https://doi.org/10.1175/MWR-D-12-00335.1

Zhang, J. A. (2010). Estimation of dissipative heating using low-level in situ aircraft observations in the hurricane boundary layer. *Journal of the Atmospheric Sciences*, *67*(6), 1853–1862. https://doi.org/10.1175/2010jas3397.1

Zhang, J. A., Black, P. G., French, J. R., & Drennan, W. M. (2008). First direct measurements of enthalpy flux in the hurricane boundary layer: The CBLAST results. *Geophysical Research Letters*, *35*(14), L14813. https://doi.org/10.1029/2008GL034374

Zhang, J. A., Drennan, W. M., Black, P. G., & French, J. R. (2009). Turbulence structure of the hurricane boundary layer between the outer rainbands. *Journal of the Atmospheric Sciences*, *66*(8), 2455–2467. https://doi.org/10.1175/2009JAS2954.1

Zhang, J. A., & Drennan, W. M. (2012). An observational study of vertical eddy diffusivity in the hurricane boundary layer. *Journal of the Atmospheric Sciences*, *69*(11), 3223–3236. https://doi.org/10.1175/JAS-D-11-0348.1

Zhang, J. A., Kalina, E. A., Biswas, M. K., Rogers, R. F., Zhu, P., & Marks, F. D. (2020). A review and evaluation of planetary boundary layer parameterizations in hurricane weather research and forecasting model using idealized simulations and observations. *Atmosphere*, *11*(10), 1091. https://doi.org/10.3390/atmos11101091

Zhang, J. A., Marks, F. D., Montgomery, M. T., & Lorsolo, S. (2011). An estimation of turbulent characteristics in the low-level region of intense Hurricanes Allen (1980) and Hugo (1989). *Monthly Weather Review*, *139*(5), 1447–1462. https://doi.org/10.1175/2010mwr3435.1

Zhang, J. A., Rogers, R. F., & Tallapragada, V. (2017). Impact of parameterized boundary layer structure on tropical cyclone rapid intensification forecasts in HWRF. *Monthly Weather Review*, *145*(4), 1413–1426. https://doi.org/10.1175/MWR-D-16-0129.1

Zhu, P. (2008). Simulation and parameterization of the turbulent transport in the hurricane boundary layer by large eddies. *Journal of Geophysical Research*, *113*(D17), D17104. https://doi.org/10.1029/2007JD009643

Zhu, P., Menelaou, K., & Zhu, Z. (2014). Impact of subgrid-scale vertical turbulent mixing on eyewall asymmetric structures and mesovortices of hurricanes. *Quarterly Journal of the Royal Meteorological Society*, *140*(679), 416–438. https://doi.org/10.1002/qj.2147

Zhang, J. A., & Rogers, R. F. (2019). Effects of parameterized boundary layer structure on hurricane rapid intensification in shear. *Monthly Weather Review*, *147*, 853–871. https://doi.org/10.1175/MWR-D-18-0010.1

Zhang, J. A., Nolan, D. S., Rogers, R. F., & Tallapragada, V. (2015). Evaluating the impact of improvements in the boundary layer parameterization on hurricane intensity and structure forecasts in HWRF. *Monthly Weather Review*, *143*, 3136–3155. https://doi.org/10.1175/MWR-D-14-00339.1